Supporting information

3D-printed Polymer Composite Devices Based on a Ferroelectric Chiral Ammonium Salt for High-Performance Piezoelectric Energy Harvesting

Supriya Sahoo,[a] *Premkumar Anil Kothavade,*[b,c] *Dipti R. Naphade,*[d] *Arun Torris,*[b,c] *Balu Praveenkumar,*[e] *Jan K. Zaręba,*[f,*] *Thomas D. Anthopoulos,*[d,*] *Kadhiravan Shanmuganathan,*[b,c,*] *Ramamoorthy Boomishankar* [a,*]

[a]Department of Chemistry and Centre for Energy Science, Indian Institute of Science Education and Research (IISER), Pune, Dr. Homi Bhabha Road, Pune – 411008, India
E-mail: boomi@iiserpune.ac.in
[b]Polymer Science and Engineering Division, CSIR-National Chemical Laboratory, Dr. Homi Bhabha Road, Pune, 411008, Maharashtra, India
[c]Academy of Scientific and Innovative Research (AcSIR), Ghaziabad, 201002, India
E-mail: k.shanmuganathan@ncl.res.in
[d]King Abdullah University of Science and Technology (KAUST), KAUST Solar Center (KSC), Thuwal 23955-6900, Saudi Arabia
E-mail: thomas.anthopoulos@kaust.edu.sa
[e]PZT Centre, Armament Research and Development Establishment, Dr. Homi Bhabha Road, Pune – 411021, India
E-mail: praveen0406@gmail.com
[f]Institute of Advanced Materials, Wrocław University of Science and Technology, Wrocław-50-370, Poland
E-mail: jan.zareba@pwr.edu.pl

CCDC No. 2235772 (1_120K) and 2235773 (1_298K)

Table of contents

EXPERIMENTAL SECTION

General Remarks

S-3,3-dimethyl-2-butylamine was purchased from Sigma Aldrich and was used without further purification. Tetrafluoroboric acid was purchased from Avra Chemicals. Polycaprolactone (PCL) was purchased from Sigma Aldrich and was used as received. The thermogravimetric analyses were performed using the PerkinElmer STA-6000 analyzer at a heating rate of 10 °C/min in a nitrogen atmosphere. Differential scanning calorimetry (DSC) measurements were performed on a TA Q20 differential scanning calorimeter with heating and cooling rates of 10 °C/min under the nitrogen atmosphere. NMR spectra were recorded on a Bruker 400 MHz spectrometer (1 H NMR, 400.13 MHz; 13C{1 H} NMR, 100.62 MHz) in $CDCl_3$ solvent. Melting point analyses were done using a Buchi M-560 melting point apparatus and were uncorrected. The FT-IR spectrum was performed using a Perkin-Elmer spectrometer with samples prepared as KBr pellets in the ranges between 400 and 4000 cm^{-1}. The variable temperature powder X-ray diffraction (VT-PXRD) data were measured in the 2-theta range of 5 °C to 50 °C on a Bruker-D8 Advance X-ray diffractometer. The field-emission scanning electron microscopy (FE-SEM) analysis of all the composite films (all different wt%) was performed using the Zeiss ultra plus FE-SEM instrument with a minimum spatial resolution of 1 µm. The 3D X-Ray microtomography analyses were performed using a Carl Zeiss Versa 510 microscope with an applied X-ray energy of 80 kV. The Raman spectral analysis of compound **1**, neat PCL and the polymer composite films (**1**-PCL) were recorded by using a Horiba Jobin Yvon Raman spectrometer with a 50X objective lens. The compound **1** and **1**-PCL composite devices were exposed to different humid conditions using ESPC SH-222 Bench-Top Type Temperature and Humidity Chamber. The static mechanical testing (stress-strain behavior) of pure PCL and the polymeric composite films was performed on an Instron 5943 model Universal Testing Machine (UTM) using rectangular film strips (0.2 mm thickness, 5 mm width, and 30 mm overall length) at 50 mm/min strain rate and 1kN load cell.

Synthesis of 1:

To a stirred solution of HBF_4 (1 g, 2.80 mmol) in methanol (10 mL), (S)-3,3-dimethyl-2-butyl amine (0.312 g, 1.40 mmol) in methanol (10 mL) was added slowly over a period of 30 minutes. The reaction mixture was subsequently stirred for 1 hour at room temperature. The obtained clear solution was filtered through a thick pad of celite and kept for crystallization at room temperature. White crystals of **1** were obtained after 7 days. A quick comparison of the optical rotation values indicates that the chirality of compound **1** is probably changed from that of the precursor (S)-3,3-dimethyl-2-butylamine in their bulk methanolic solution. However, we are unable to confirm the chirality of the compound as it was inactive for circular dichroism (CD) measurements. Yield: 89 %. Melting point: 510-518 K. ^1H NMR (400 MHz, $CDCl_3$) δ 3.20 (q, J = 6.8 Hz, 1H), 1.31 (d, J = 6.8 Hz, 3H), 1.02 (s, 9H). ^{13}C NMR (101 MHz, $CDCl_3$) 58.07 (s), 33.05 (s), 25.36 (s), 14.03 (s). FT-IR data in KBr pellet (cm^{-1}): 3245, 2962, 1613, 1516, 1390, and 1008. Anal. Calcd. for $C_6H_{16}BF_4N$: C 38.18; H 8.53; N 7.41. Found: C 38.17; H 8.54; N 7.43.

Single Crystal X-ray Diffraction Analysis:

The single-crystal X-ray diffraction data for **1** at 120 K and 298 K were obtained on a Bruker Smart Apex Duo diffractometer using Mo Kα radiation (λ=0.71073Å). Crystal structures were solved using the direct method and then refined by full-matrix least-squares against F^2 using SHELXL-2014/7 built in the Apex 3 program.[1] All the nonhydrogen atoms were refined anisotropically. Hydrogen atoms were constructed in geometric positions to their parent atoms.[2] The structure was refined as the two-component racemic twin. The fluorine atoms of the BF_4 anions in the 298 K data were disordered. Atom positions of the disordered fragments were refined for similar distances and U-restraints using the SIMU/SAME/SADI routine of the SHELX. The structural illustrations were prepared by using DIAMOND-3.1 software.

Hirshfeld Surface Analysis:

The Hirshfeld surface analysis was mapped with d_{norm} and 2D fingerprint plots using Crystal Explorer 3.1 program. For this study, the single-crystal X-ray crystallographic information file (CIF) was utilized to visualize all the different types of interactions present on the Hirshfeld surface. These interactions were obtained as 3D color mapping images such as normalized contact distance (d_{norm}), shape index, and curvedness. The diverse surface color mappings of **1** were generated on the Hirshfeld surface by different color coding based on intense (red), medium (blue), and weak (white) interactions. The 2D fingerprint plot is in fact a histogram which can be constructed by compiling all the distances of given atoms that are nearest to the interior (d_i) and exterior (d_e) of the generated Hirshfeld surface. The different contours (blue and grey color) that are present in the 2D fingerprint plot explain the various types of molecular interactions.

Nonlinear Optical Measurements:

Nonlinear optical measurements was performed by using a direct output from a Coherent Astrella Ti:Sapphire regenerative amplifier providing femtosecond laser pulses (800 nm, 75 fs) at a 1 kHz repetition rate. The output was used unfocused. Laser fluence at samples was equal to 0.28 mJ/cm^2.

In order to perform a Kurtz-Perrywder test, the single crystals of of **1** and KDP were crushed with a spatula and sieved through an Aldrich mini-sieve set, collecting a microcrystal size fraction of 125–177 µm. Next, size-graded samples were fixed in-between microscope glass slides to form tightly packed, uniform layers, sealed, and mounted to the horizontally aligned sample holder. No refractive index matching oil was used. Under the same excitation conditions, the SHG signal was collected for **1** and KDP for 6000 ms and 500ms, respectively.

The employed measurement setup operates in the reflection mode. Specifically, the laser beam delivered from the regenerative amplifier, passed through a 5mm aperture, was directed onto the sample at 45 degrees to its surface. Emission collecting optics consisted of a Ø25.0 mm plano-convex lens of focal length 25.4 mm mounted to the 400 µm 0.22 NA glass optical fiber and was placed along the normal to the sample surface. The distance between the collection lens and the sample was equal to 30 mm. The spectra of SHG responses were recorded by an Ocean Optics Flame T fiber-coupled CCD spectrograph with a 200 µm entrance slit. Scattered pumping radiation was suppressed with the use of a Thorlabs 750 nm short pass dielectric filter (FESH0750).

In the case of temperature-resolved measurement, the same geometry of the experimental setup was employed. The temperature control of the sample was realized (dT/dt = 5K/min) using a Linkam LTS420 Heating/Freezing Stage. Temperature stability was equal to 0.1 K.

Ferroelectric, Dielectric and Piezoelectric Measurements:

The *P-E* hysteresis loop measurements on **1** were performed on its compact disc sample with approximately 8 mm diameter and 1.2 mm thickness electroded with Cu adhesive tapes. The ferroelectric polarization vs. electric field (*P-E*) measurements were performed on the aixACCT TF-2000E model hysteresis loop analyzer. The leakage currents were dynamically recorded during the hysteresis loop measurements.

The dielectric permittivity measurement were performed on the powder pressed pellet of **1**. The measurements were performed using the Solartron Analytical Impedance Analyzer model 1260 coupled with a Dielectric Interface 1296A operating with Janis 129610A cryostat sample holder and a Lakeshore 336 model temperature controller.

The piezoelectric nature of **1** was again confirmed from the d_{33} measurements using the Berlincourt Piezotest meter model PM300 on the compacted disc of **1** with approximately 8 mm diameter and 1.2 mm thickness.

Dipole Moment Calculations:

The polarization exhibited by these two materials was further confirmed from the preliminary theoretical dipole moment ONIOM calculations performed by using the Gaussian 09 program. For this calculation, the anionic parts were taken as the high layer, and the cationic parts were regarded as the lower layer. These dipole moment (ONIOM) calculations were performed using the Density Functional Theory (DFT) method.[3]

Piezoresponse Force Microscopy Characterizations:

The ferroelectric domain structure of **1** thin film and its micro crystals were done using a commercial AFM system [MFP 3D, Asylum Research in the contact mode (vector mode)]. The vertical and lateral domain orientations were probed by using the Pt/Ir coated tip [SCM-PIT-V2 by Bruker) with spring constant of 2.8 N/m and tip radius of 25 nm and imaging were done by using Pt-coated silicon probe. To enhance the signal, resonant enhanced PFM mode was used with a frequency of 285 KHz and AC amplitude of 2 V. The switching ability of the domains on thin films was checked by the application of external DC bias of ±40 and ±60 V using the PFM tip in contact mode. The thin films of the compound were prepared by drop casting 40 mg of the compound **1** in 1 ml Methanol and drop cast it on the substrate followed by annealing at room temperature for 30 minutes.

General Procedure for the Preparation of Polymer Composite Films and Devices:

The composite films of **1** were prepared by dissolving 5, 10, 15 and 20 wt% of the ferroelectric crystallites into nonpiezoelectric biodegradable polycaprolactone (PCL) in dimethylformamide (DMF) solution. Homogeneous solutions were prepared by keeping the solutions for mechanical stirring at 50 ˚C for 15 min, followed by vortex mixing for 15 min. The homogeneous solutions were poured onto a glass slide and kept undisturbed in an oven at 50 ˚C for 3 h. The dried free-standing composite films comprising 5, 10, 15, and 20 wt% of **1** in PCL were subsequently peeled off from the glass slide. To perform the energy harvesting applications on **1**-PCL composite films, the device structures were made by placing adhesive copper contacts on either side of the film and soldering Cu-wires (0.3 mm) to the contact strips. The device architectures were completed by covering them with Kapton tapes, which protect the devices from the impact force and minimize the static charge developed during the piezoelectric measurement.

General Procedure for the Preparation of 1-PCL Filaments:

All **1**-PCL composite filaments were prepared by solution mixing followed by melt extrusion. **1**-PCL composite films that were prepared as per the protocol mentioned above were shredded and then melt compounded in a Haake Mini CTW twin-screw extruder at 110 °C for 3 min. Subsequently filament having a diameter of 2.75 ±0.2 mm was extruded from the die of the extruder by optimizing the screw and take up roller speed.

Procedure for the Preparation of 3D printed Polymer Composite Devices:

Prior to 3D printing, the prepared **1**-PCL composite filaments were dried in a vacuum oven at ambient temperature for 24 h. Ultimaker 3 FDM type 3D printer was used to print 3D shapes with different infill patterns (Zig-zag, grid, gyroid and triangular). The optimal printing conditions for ***Gy*-1**-PCL composite are given below.

Table S1. The optimal printing conditions for ***Gy*-1**-PCL composite.

Process Parameters	Values
Bed	Glass plate
Nozzle size (mm)	0.4
Nozzle temperature (°C)	120
Bed temperature (°C)	30
Infill degree (%)	50
Layer height (mm)	0.1
Flow (%)	100
Print speed (mm/s)	30

Piezoelectric Energy Harvesting and Storage Measurements:

The mechanical energy harvesting experiments were conducted on a custom-built periodic impact instrument operating at an impact force of 21 N and frequency of 10 Hz (Picture S1). The output voltages and currents were measured using a Tektronix 2024 Mixed Signal Oscilloscope operating at an input impedance of 1 MΩ. The thickness and the active area of the devices (**1**-PCL) under test were ~1mm and 360 mm^2, respectively. The thickness and area of the 3D-printed ***Gy*-1**-PCL devices were ~2mm and 600 mm^2 respectively. The energy storage attributes of the 10 wt% **1**-PCL and ***Gy*-1**-PCL devices during impact measurements were tested with a 100 μF capacitor by connecting the devices and the capacitor with a full wave-bridge four-diode circuit.

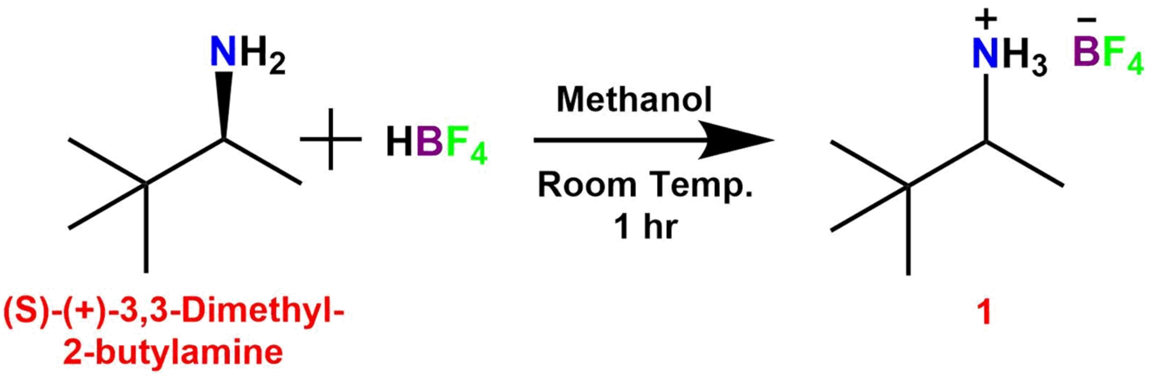

Scheme S1. Synthesis of **1**.

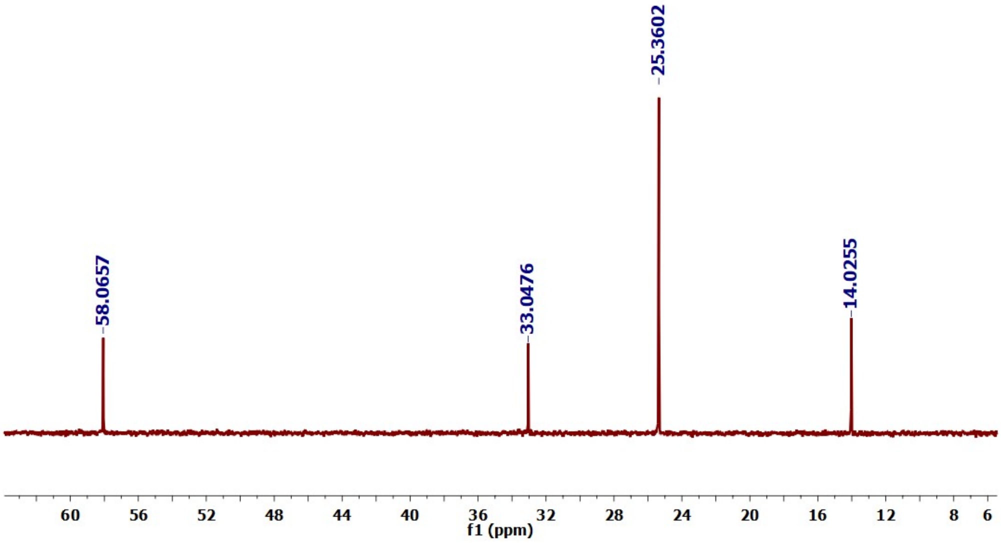

Figure S1. ^{13}C Spectrum of **1**.

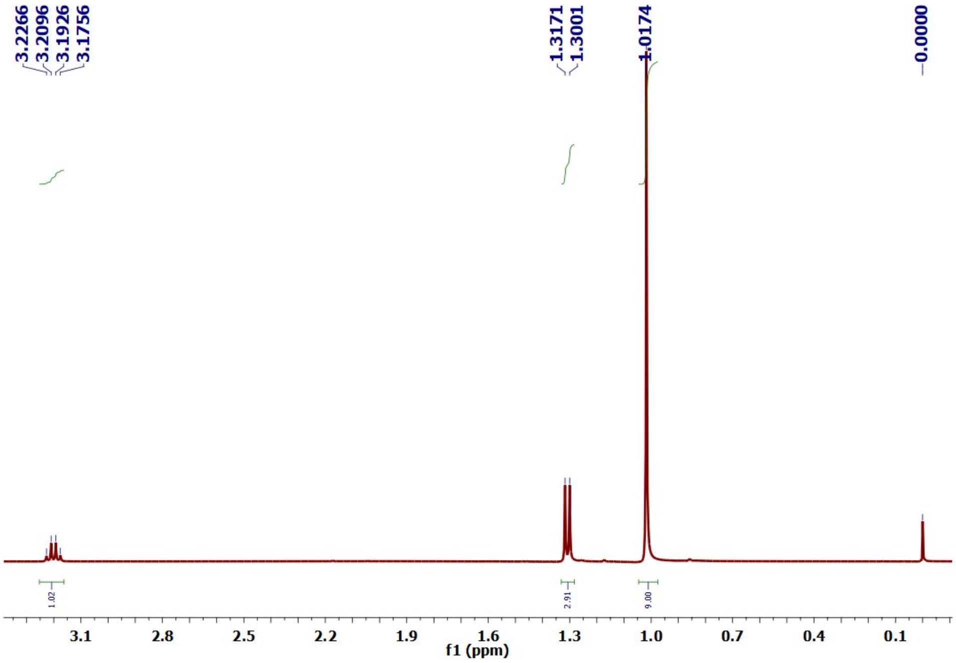

Figure S2. ^{1}H Spectrum of **1**.

Table S2. X-ray Crystallographic data for **1**.

Crystallographic details	**120 K**	**298 K**
Chemical formula	$C_6H_{16}BF_4N$	$C_6H_{16}BF_4N$
Formula weight (g/mol)	189.01	189.01
Temperature	120(2)K	298(2)K
Crystal system	Tetragonal	Tetragonal
Space group	$P4_2$	$P4_2$
a (Å); α (°)	15.808(3); 90	15.93(3); 90
b (Å); β (°)	15.808(3); 90	15.93(3); 90
c (Å); γ (°)	7.9627(18); 90	8.241(16); 90
V (Å^3); Z	1989.9(10); 8	2090(9); 8
ρ (calc.) g cm^{-3}	1.262	1.201
μ (Mo K$_\alpha$) mm^{-1}	0.125	0.119
2θ_{max} (°)	50.484	45.024
R(int)	0.0922	0.1843
Completeness to θ	100	99.9
Data / param.	4973/174	2748/300
GOF	1.550	1.023
R1 [F>4σ(F)]	0.0995	0.0850
wR2 (all data)	0.2673	0.2837
max. peak/hole (e.Å^{-3})	0.954/-0.645	0.296/-0.190
Flack parameters	0.0(4)	-0.3(10)

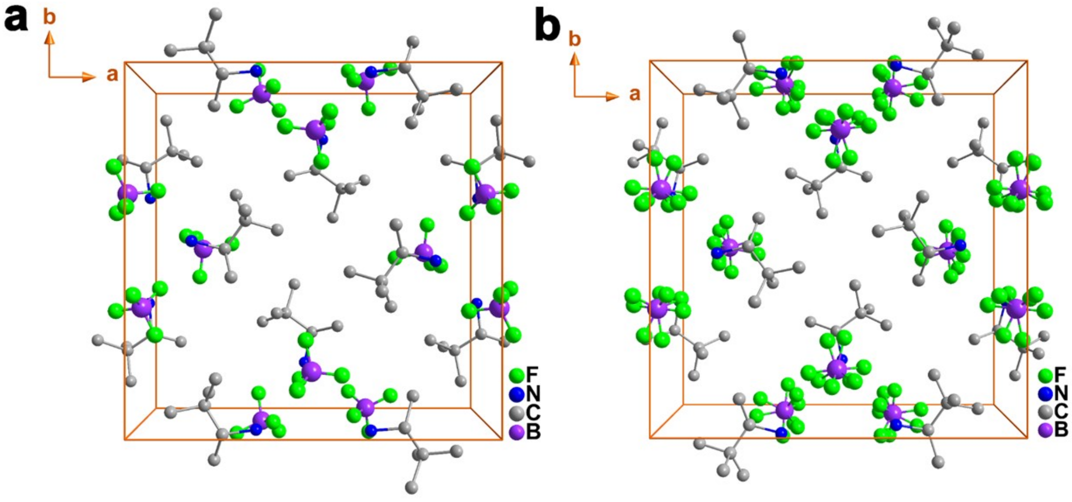

Figure S3. Packing diagrams of **1** along c-axis at (a) 120 K and (b) 298 K.

Table S3. Hydrogen bonding parameters for **1** at 120 K.

D-H···A	d(H···A) Å	d(D-A) Å	<(DHA)	Symmetry transformations to generate equivalent atoms
N(11)-H(11A)···F21	1.9894(93)Å	2.7835(132) Å	144.975(654)	x, y, 1+z
N(21)-H(21C)···F12	2.0595(103)Å	2.8767(137) Å	148.911(639)	1-x, 2-y, 1+z
N(21)-H(21A)···F22	1.9522(65)Å	2.8576(135) Å	172.589(766)	1-x, 2-y, 1+z
N(11)-H(11C)···F14	2.0209(96)Å	2.9301(141) Å	176.445(703)	x, y, 1+z
N(21)-H(21B)···F13	1.9849(100)Å	2.8879(139) Å	170.784(643)	x, y, 1+z
N(11)-H(11B)···F24	2.1182(69)Å	2.9225(120) Å	151.374(324)	1-x, 2-y, 1+z

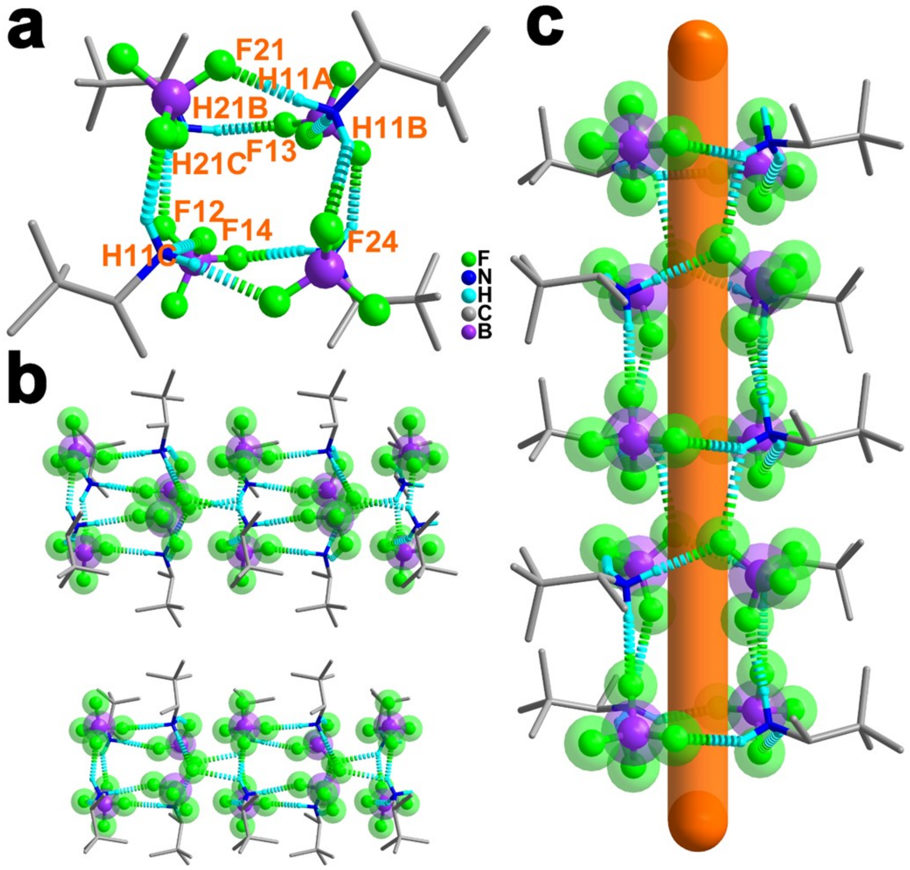

Figure S4. N-H···F hydrogen bonding interactions in **1** at 120 K. (a) View of a tetrameric core of four cations and four anions in **1**. (b) Formation of a 1D-polymeric structure via the connection between the neighbouring tetrameric motifs in the packing. (c) View of the 1D-helical structure present in **1**.

Table S4. Hydrogen bonding parameters for **1** at 298 K.

D-H···A	d(H···A) Å	d(D-A) Å	<(DHA)	Symmetry transformations to generate equivalent atoms
N(1)-H(1A)···F11’	1.9696(263)Å	2.8289(317) Å	162.038(1292)	1-x, 2-y, z
N(1)-H(1B)···F13’	2.1240(232)Å	2.9339(283) Å	150.938(1176)	1-x, 2-y, z
N(1)-H(1C)···F24	2.1715(276)Å	3.0606(245) Å	175.873(1158)	1-x, 2-y, z
N(2)-H(2A)···F23’	2.0099(247) Å	3.887(30) Å	168.465(1266)	1-x, 2-y, 1+z
N(2)-H(2B)···F21’	1.9368(292) Å	2.7617(317) Å	153.368(1371)	x, y, 1+z
N(2)-H(2C)···F14	2.1248(184) Å	2.9971(305) Å	166.353(1628)	x, y, 1+z

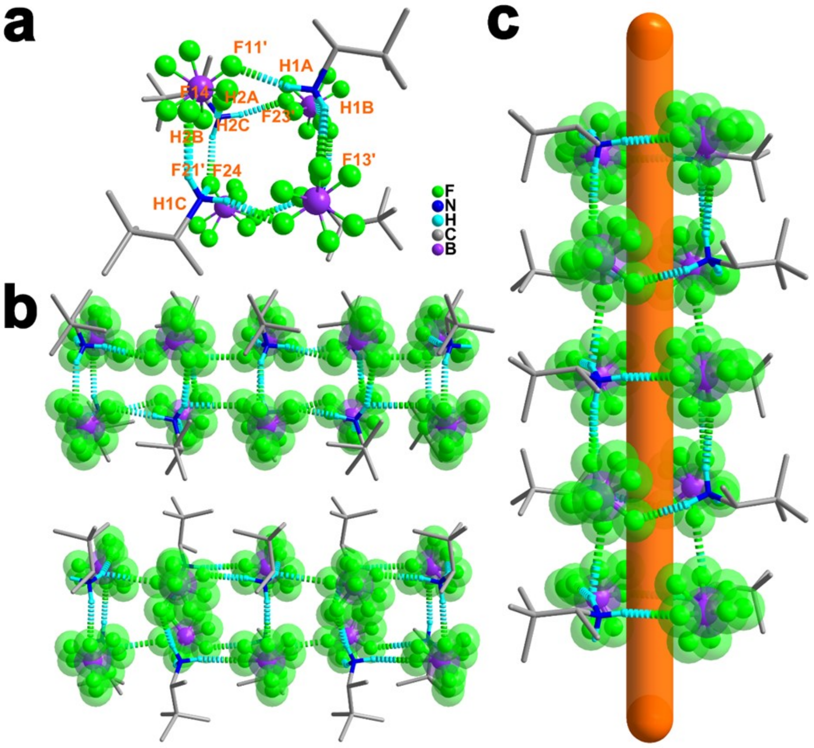

Figure S5. N-H···F hydrogen bonding interactions in **1** at 298 K. (a) View of a tetrameric core of four cations and four anions in **1**. (b) Formation of a 1D-polymeric structure via the connection between the neighbouring tetrameric motifs in the packing. (c) View of the 1D-helical structure present in **1**.

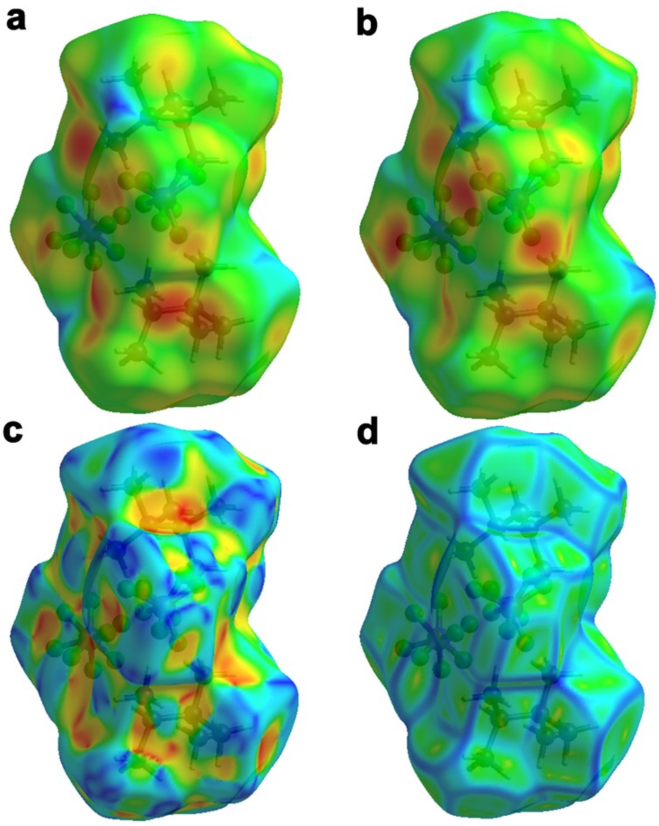

Figure S6. The 3D color mapping derived from the Hirshfeld surface analysis of **1** (298 K) showing (a) d_i, (b) d_e, (c) shape index, (d) curvedness.

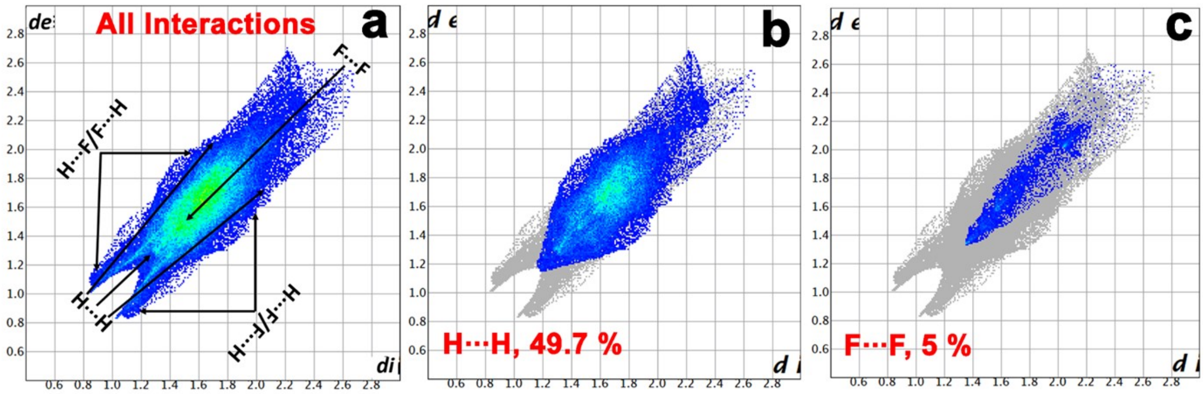

Figure S7. 2D fingerprint (d_e vs d_i) plot of **1** (298 K) showing (a) all the possible interactions and the percentages of (b) H···H and (c) F···F interactions in the molecule.

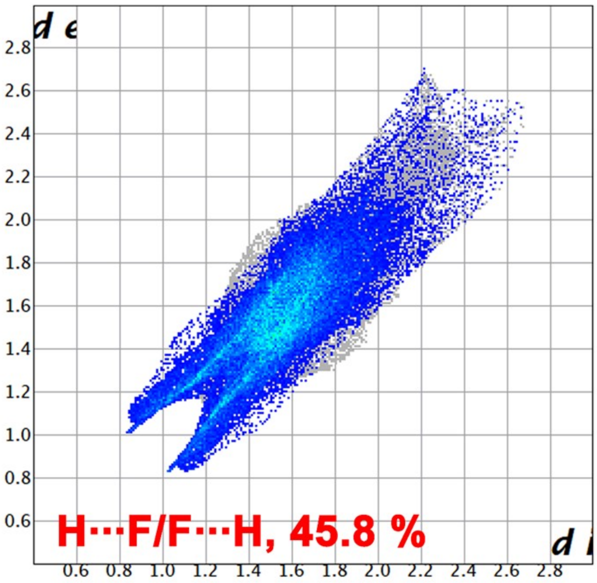

Figure S8. 2D fingerprint (d_e vs d_i) plot of **1** (298 K) showing the H···F/F···H interactions in the molecule.

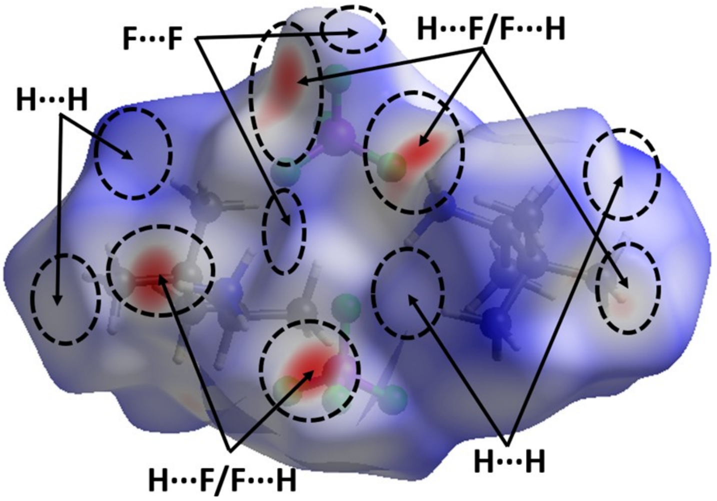

Figure S9. The 3D color mapping derived from the Hirshfeld surface analysis showing all interactions present in **1** (120 K).

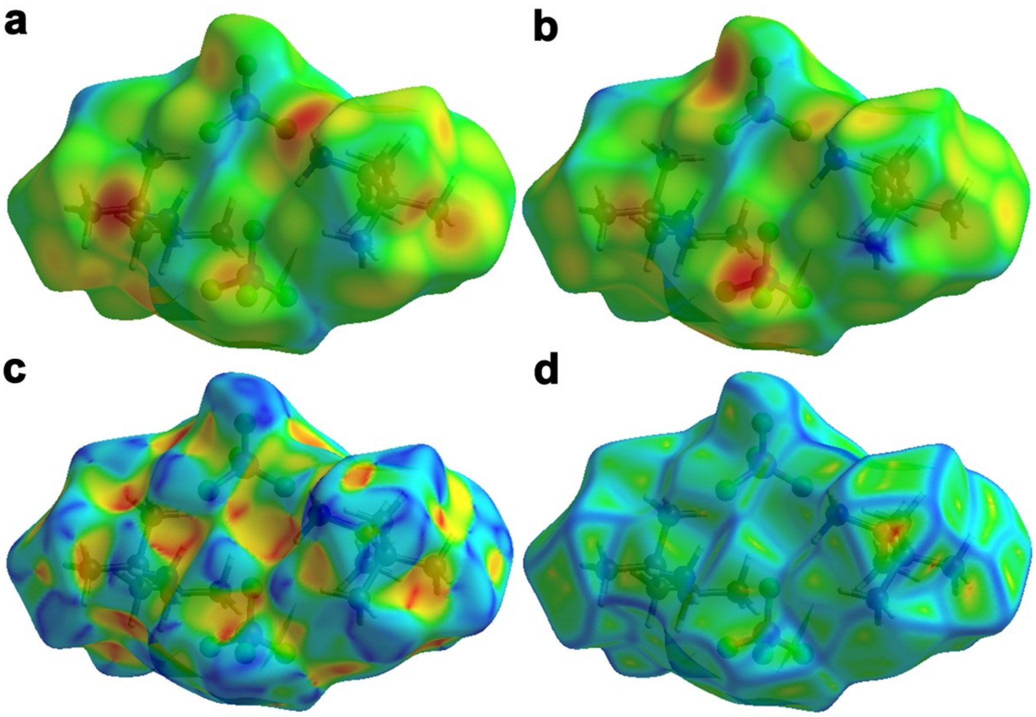

Figure S10. The 3D color mapping derived from the Hirshfeld surface analysis of **1** (120 K) showing (a) d_i, (b) d_e, (c) shape index, (d) curvedness.

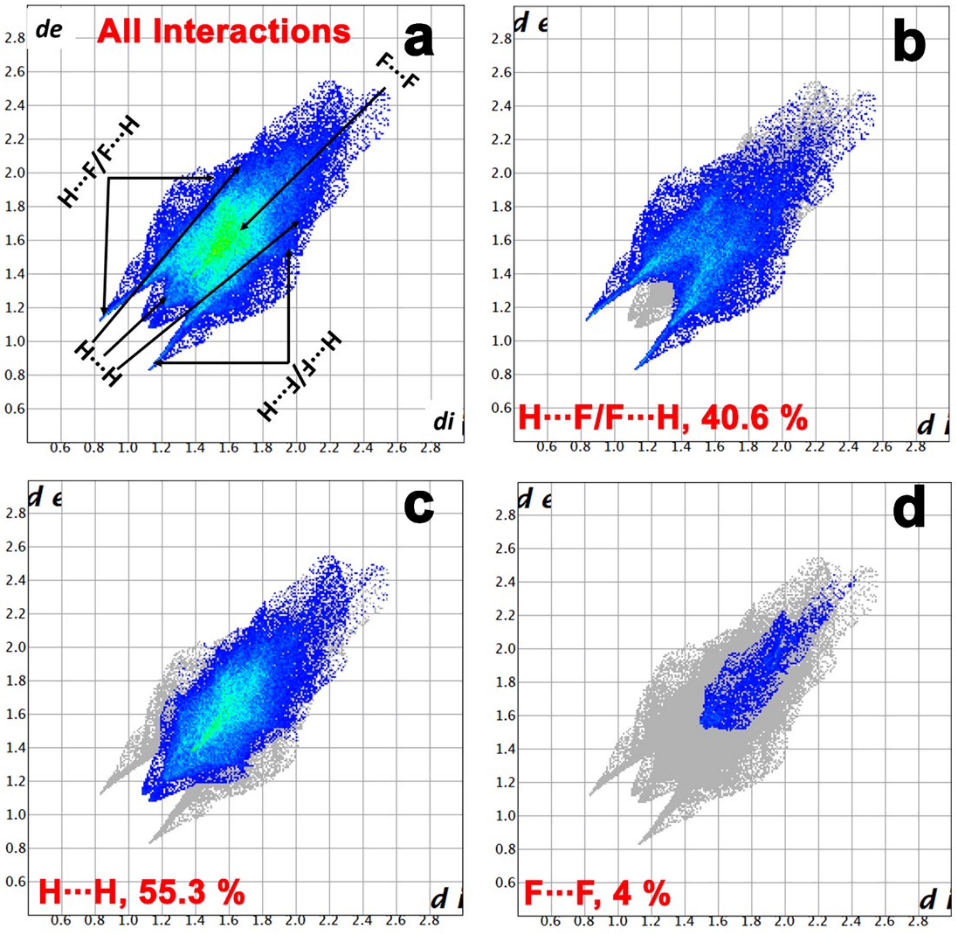

Figure S11. 2D fingerprint (d_e vs d_i) plot of **1** (120 K) showing (a) all the possible interactions and the percentages of (b) H···H and (c) F···F interactions in the molecule.

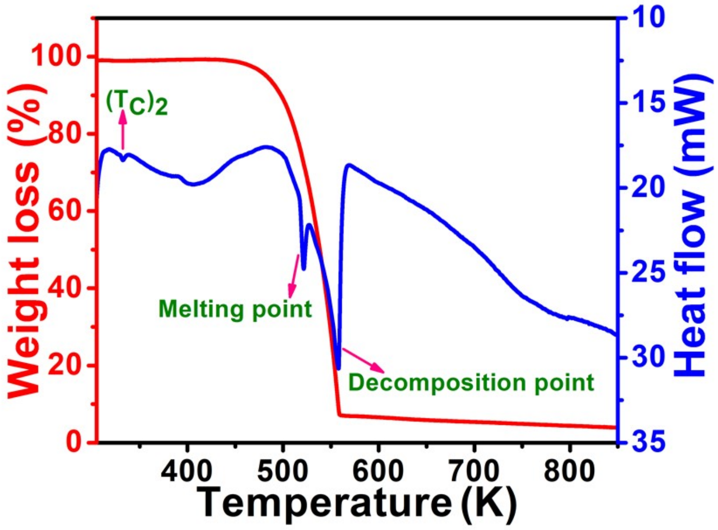

Figure S12. The thermogravimetric-differential thermal analysis profile of **1**.

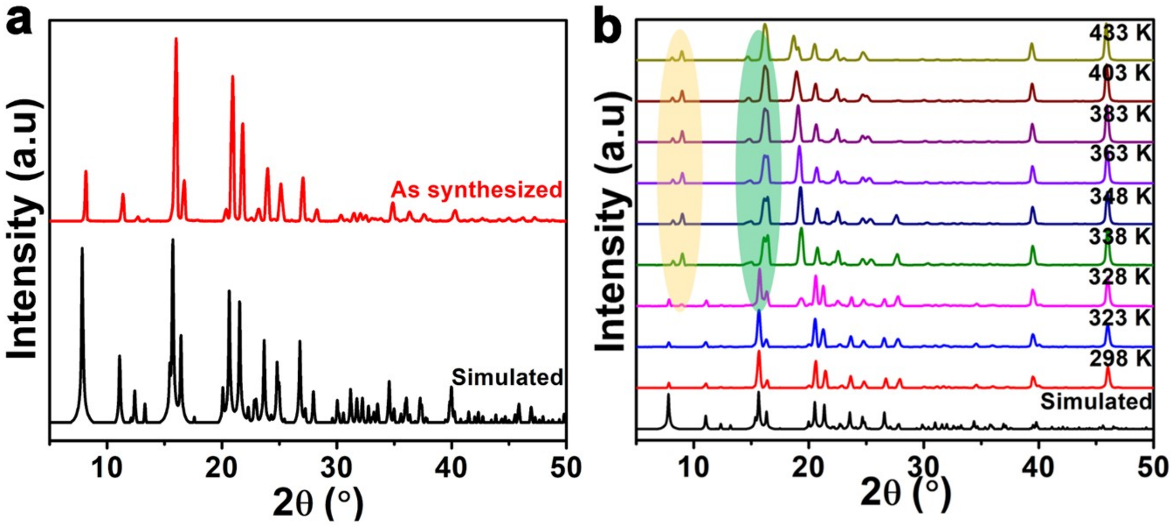

Figure S13. The (a) room temperature and (b) variable temperature powder X-ray diffraction profile of **1** along with its simulated profiles from the 298 K single-crystal data.

Table S5. Indexed PXRD unit cell parameters for **1** at HTP 348 K.

Crystal System	Tetragonal	
Space Group	$P4_22_12$	
Cell Parameters		**ESDs**
a (Å)	11.65053	0.012
b (Å)	11.65053	0.012
c (Å)	13.90133	0.022
α (°)	90	0
β (°)	90	0
γ (°)	90	0
V (Å^3)	1886.896	0

The PXRD data of **1** at 348 K was analysed using Highscore Plus software suit. McMaille method was used to index the pattern and the cell parameters were refined for zero 2-theta shift.

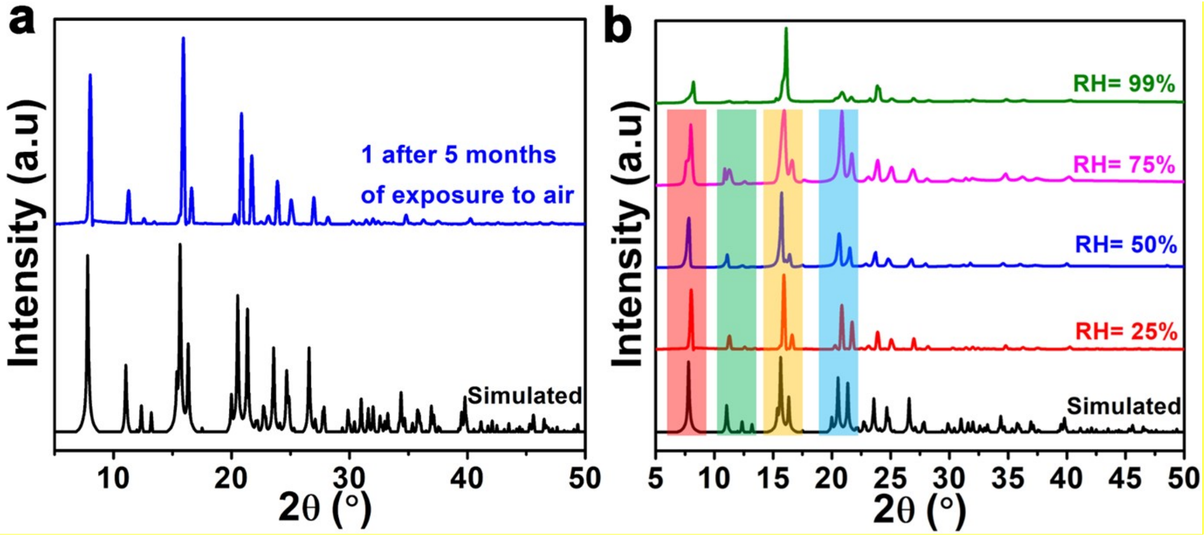

Figure S14. PXRD profile of **1** (a) after 5 months of preparation and (b) kept at different humid conditions at 298 K.

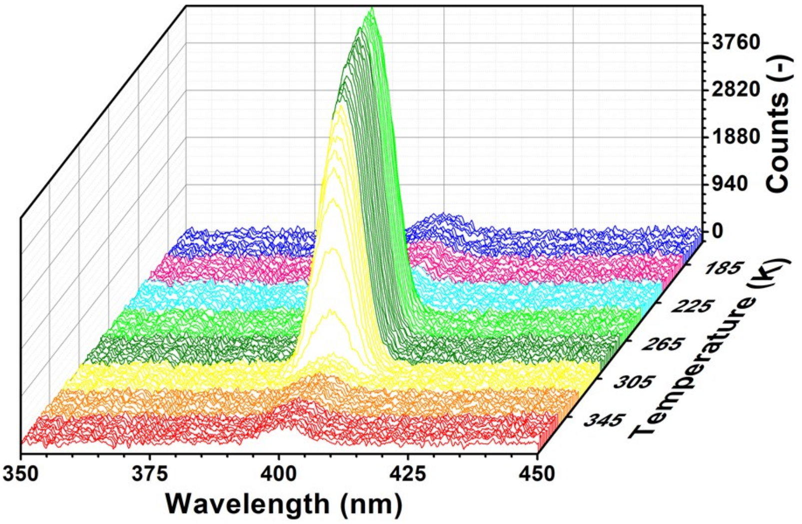

Figure S15. The temperature dependent SHG activity of **1**.

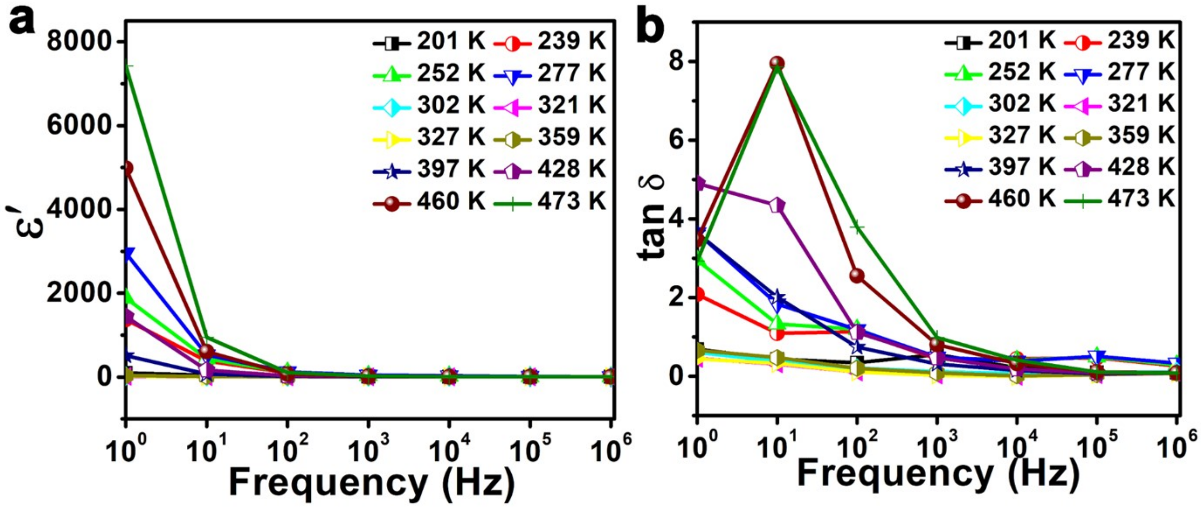

Figure S16. Frequency dependent (a) dielectric permittivity and (b) dielectric loss plots of **1**.

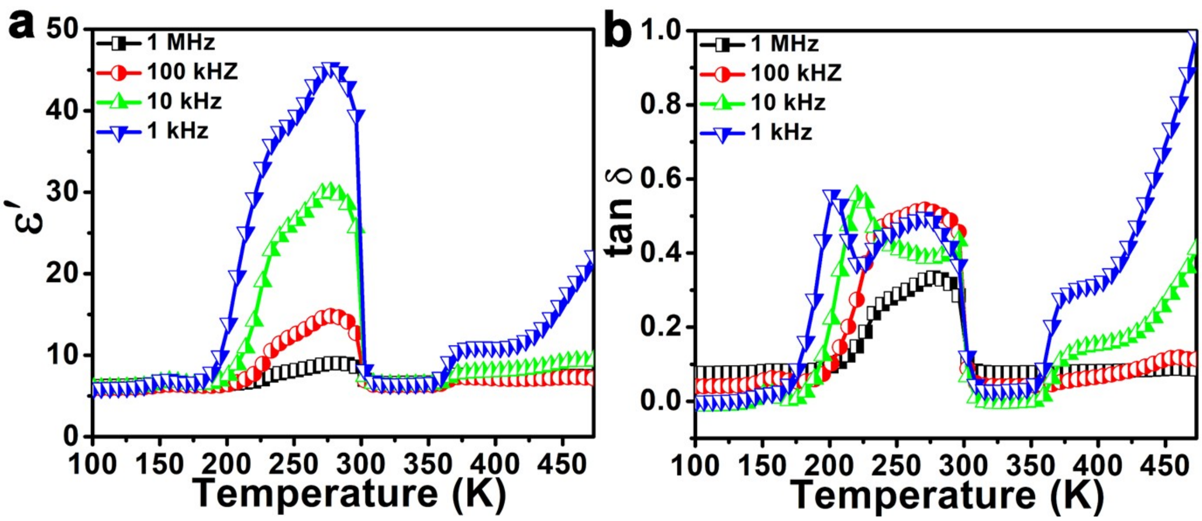

Figure S17. Temperature dependent (a) dielectric permittivity and (b) dielectric loss plots of **1**.

Table S6. Dipole moment calculation of **1**.

Temperature	Ferroelectric Material	Dipole moment in Debye unit (D)
120 K	**1**	18.4
298 K	**1**	17.7

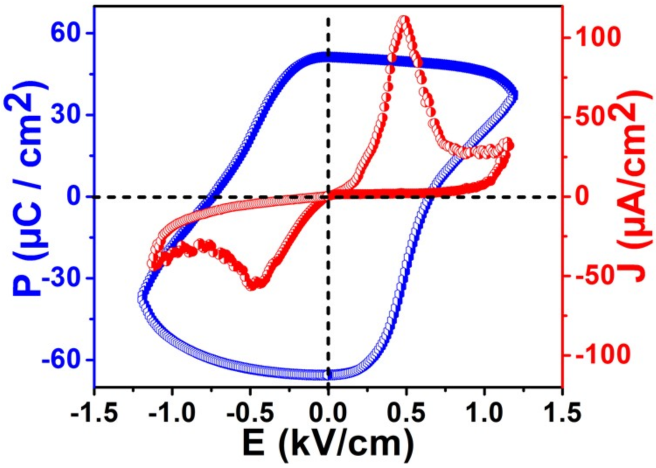

Figure S18. The P-E hysteresis analysis of **1** at 218 K showing a higher polarization value of 37.90 μC cm^{-2} at 0.1 Hz frequency with a slightly higher E_c of 0.65 kV cm^{-1}.

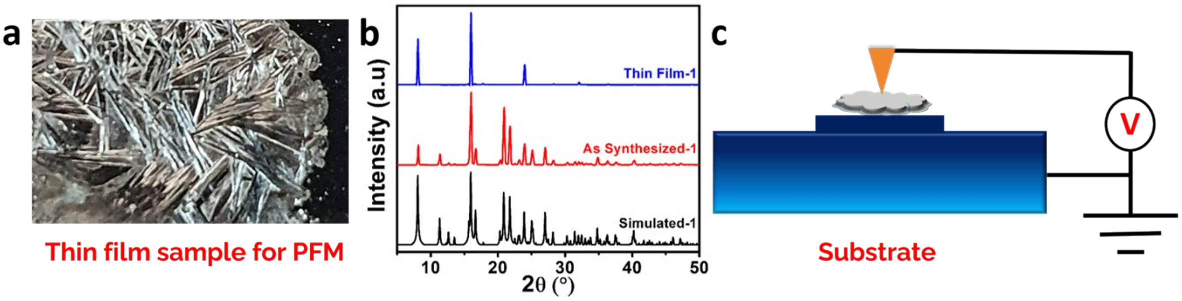

Figure S19. The thin film sample of **1** (left) employed for the PFM measurement. The schematic diagram showing the PFM experiment (right).

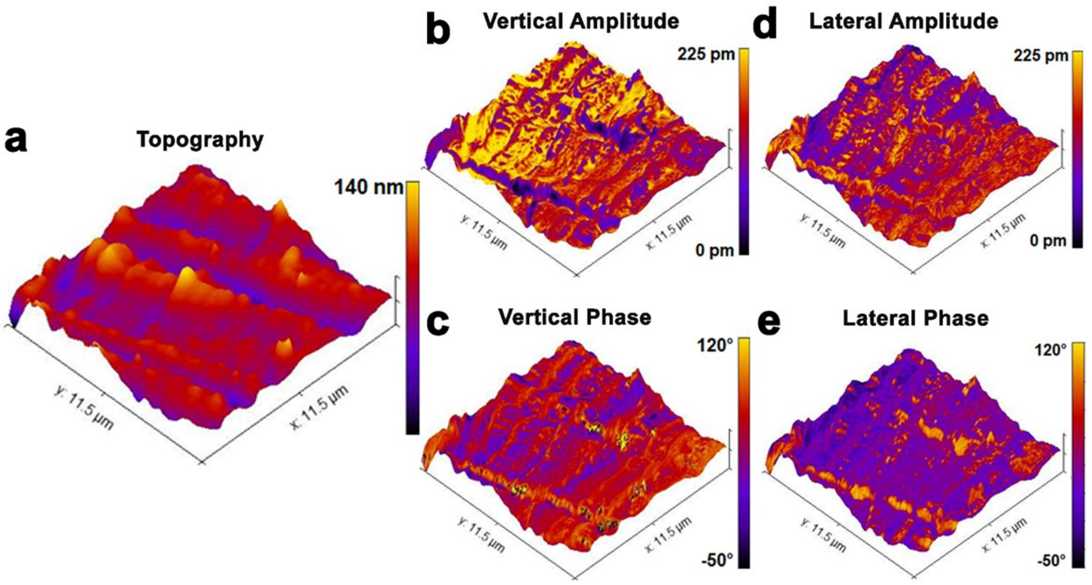

Figure S20. The vector PFM data of a thin film sample of **1** showing the (a) blank 3D-topography image (b) 3D-vertical amplitude, (c) 3D-vertical phase, (d) 3D-lateral amplitude, (e) 3D-lateral phase images over laid on the corresponding topography.

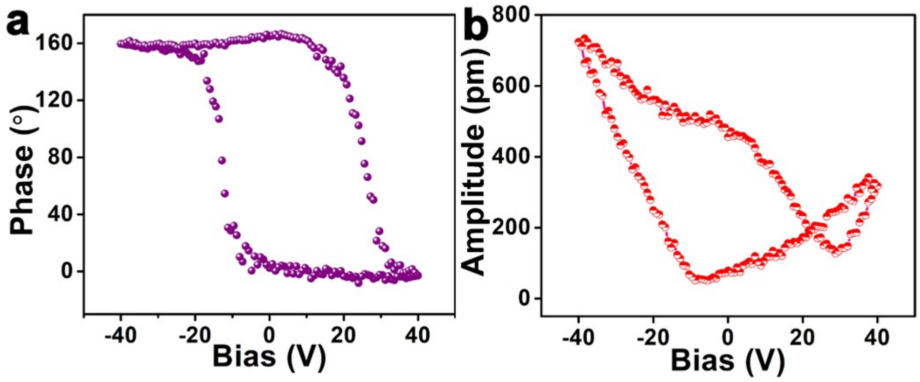

Figure S21. The ±40 V bias (a) Phase hysteresis loop and (b) Amplitude-bias butterfly loop of **1**.

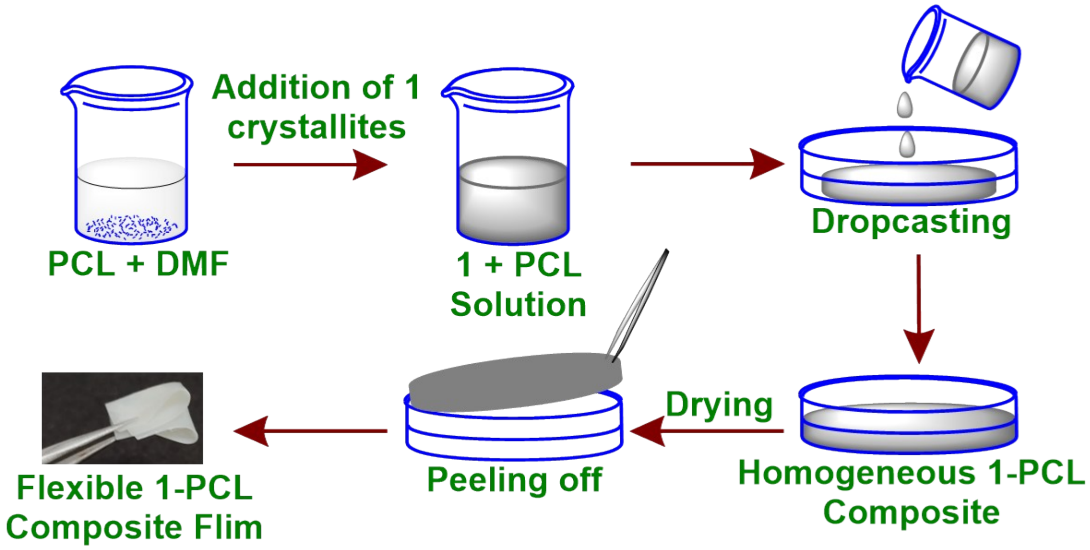

Figure S22. Schematic for the preparation of **1**-PCL composite films.

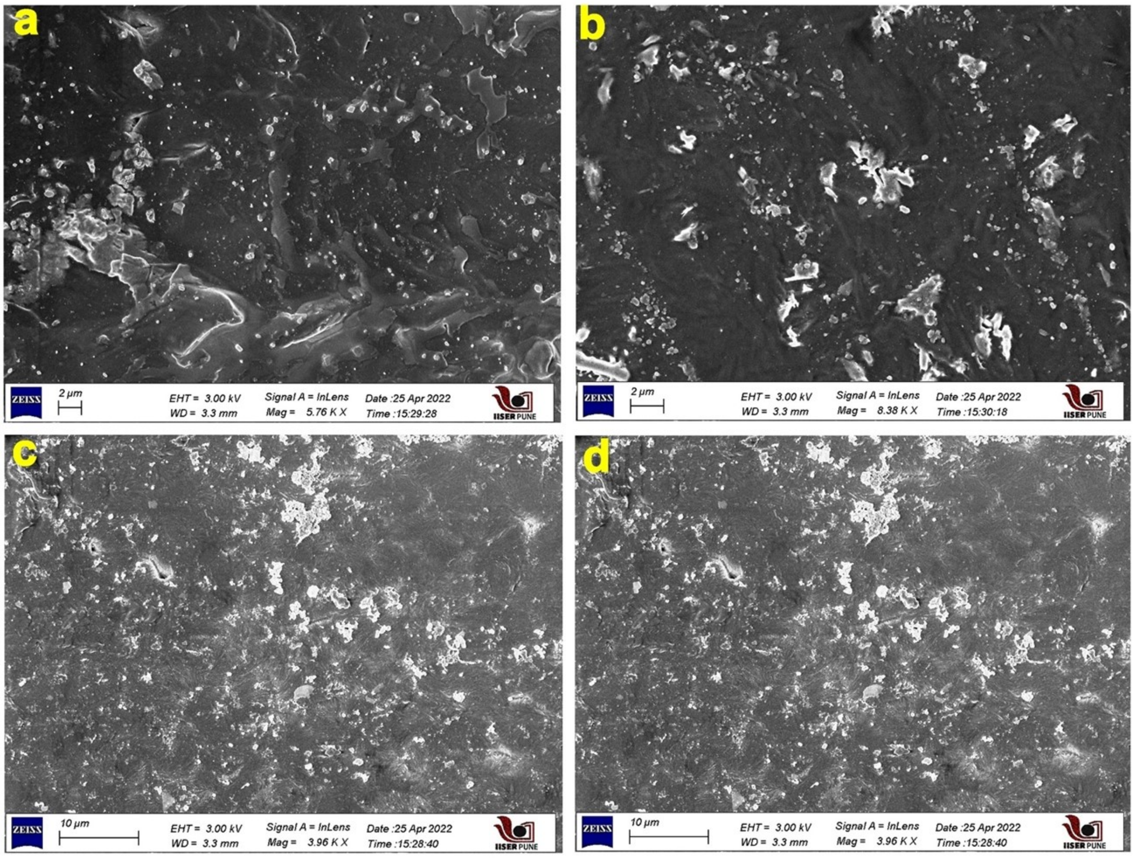

Figure S23. SEM images of 5 wt% **1**-PCL composite.

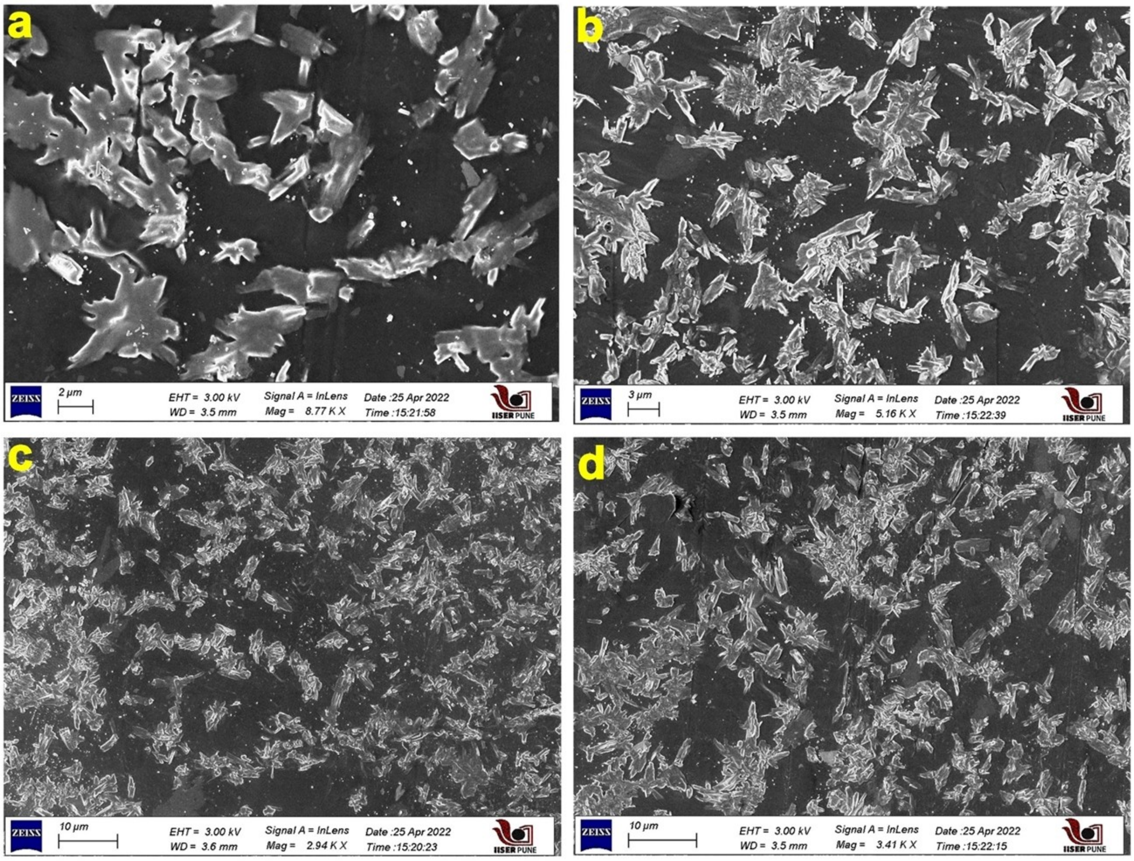

Figure S24. SEM images of 10 wt% **1**-PCL composite.

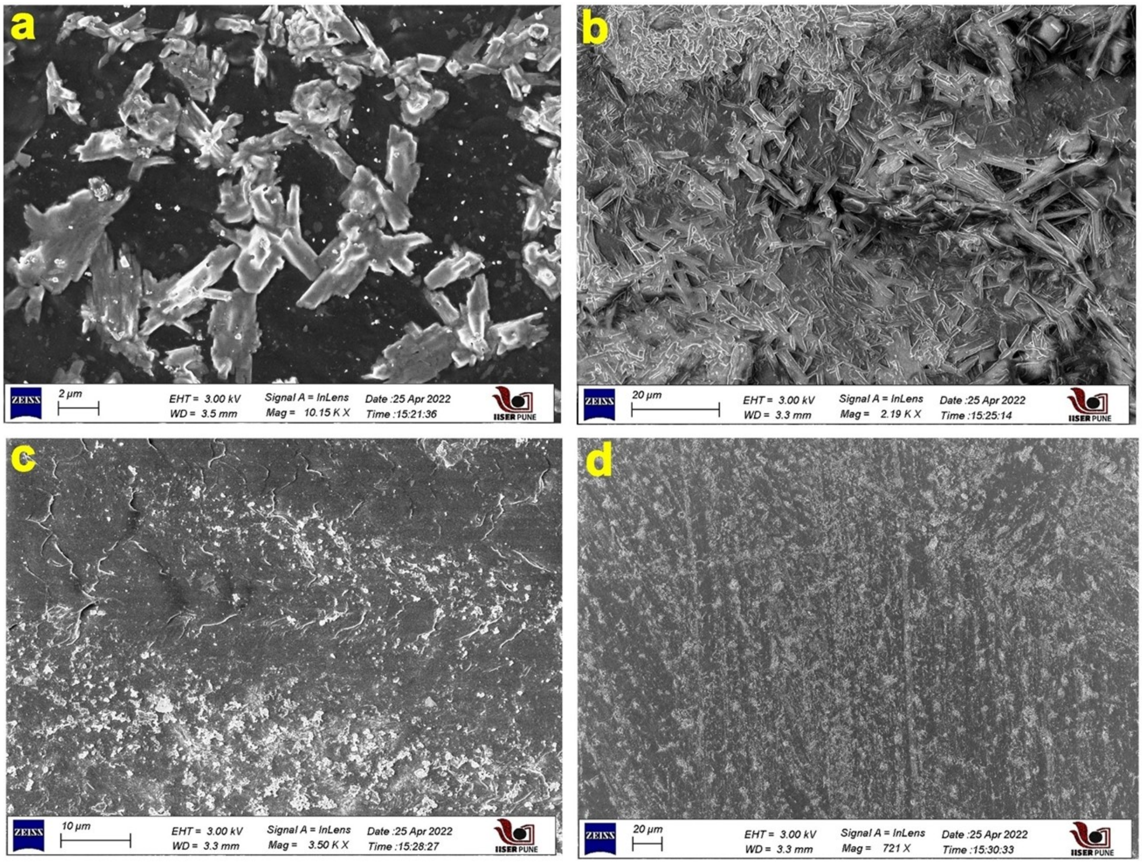

Figure S25. SEM images of 15 wt% **1**-PCL composite.

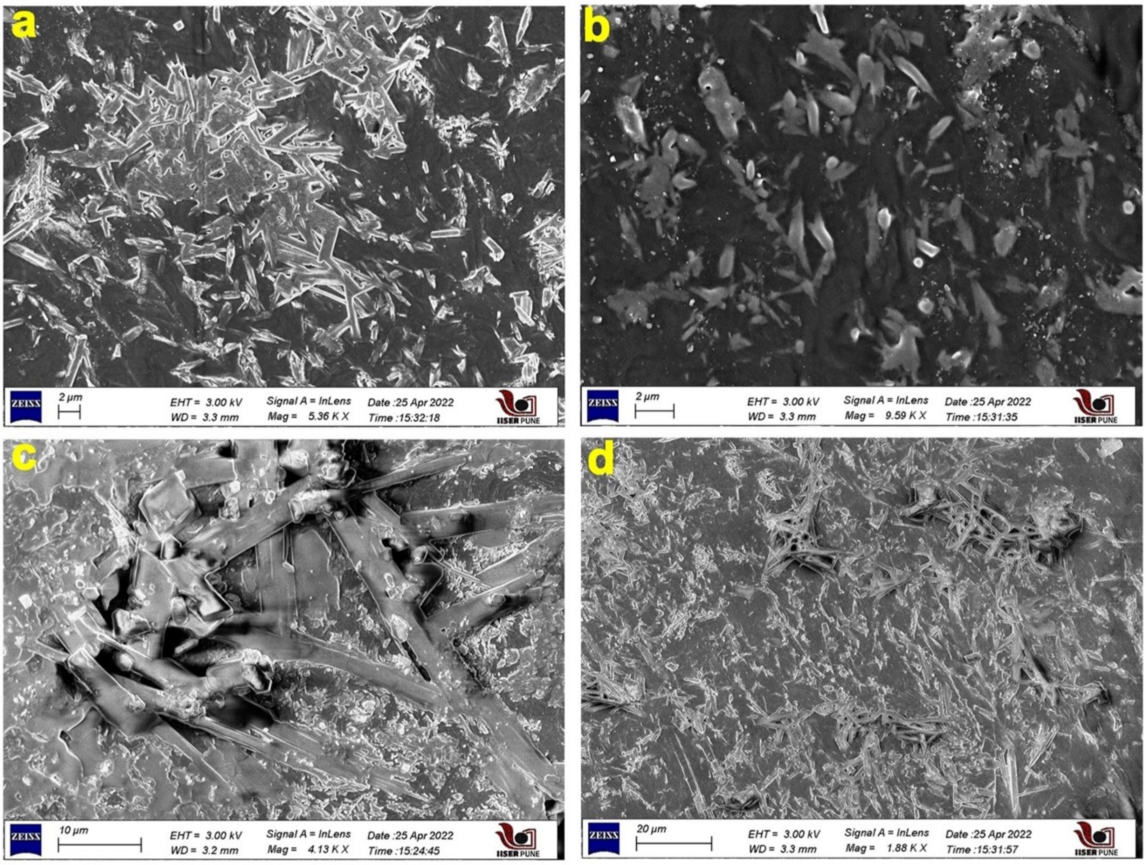

Figure S26. SEM images of 20 wt% **1**-PCL composite.

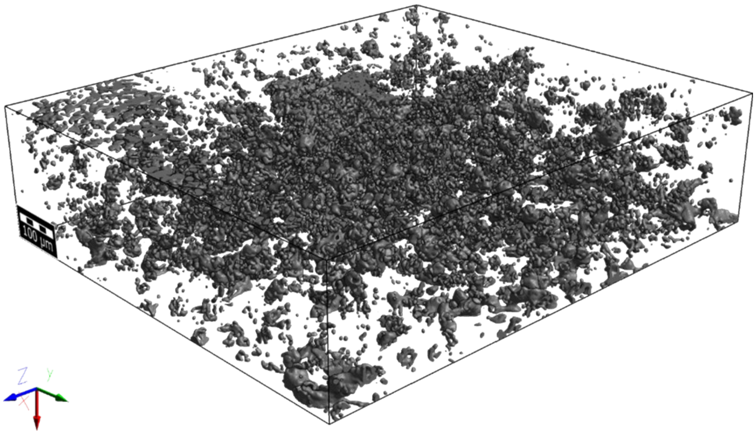

Figure S27. The 3D visualisation of the **1** crystallites in the polymer matrix of 10 wt% **1**-PCL composite film (the polymer background was corrected to visualize the spatial distribution of the crystallites of **1** in the matrix) (scale bar is 100 microns).

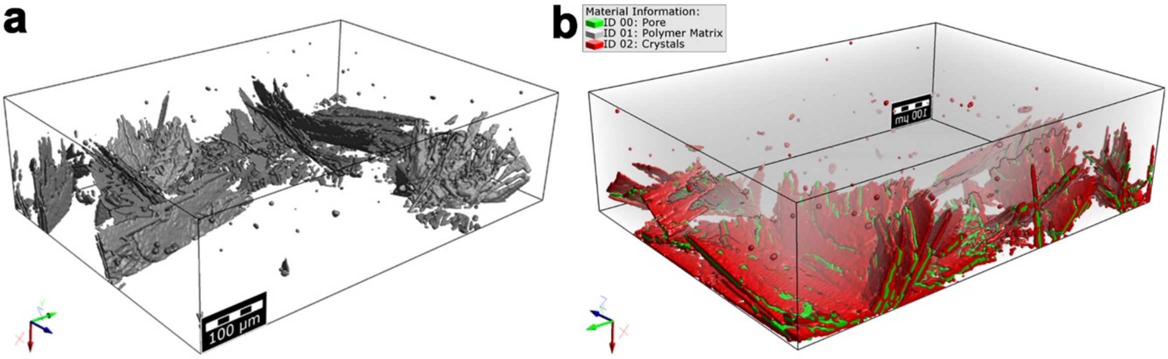

Figure S28. The X-ray 3D-microtomography (a) 3D visualisation of the **1** crystallites in the polymer matrix (the polymer background was corrected to visualize the spatial distribution of the crystallites of **1** in the matrix) and (b) 3D visualisation of the **1** crystallites along with the polymer matrix in the 5 wt% **1**-PCL composite film (red colour represents crystals and green represents void volume) (scale bar is 100 microns).

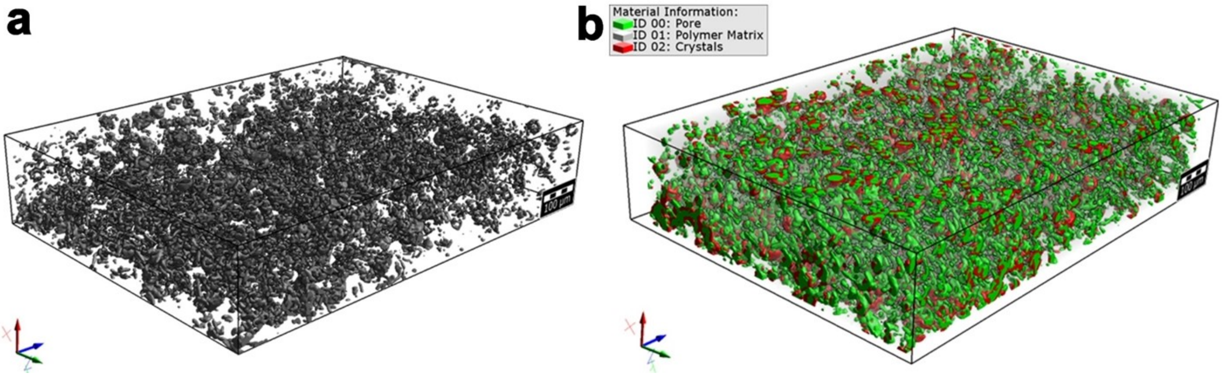

Figure S29. The X-ray 3D-microtomography (a) 3D visualisation of the **1** crystallites in the polymer matrix (the polymer background was corrected to visualize the spatial distribution of the crystallites of **1** in the matrix) and (b) 3D visualisation of the **1** crystallites along with the polymer matrix in the 20 wt% **1**-PCL composite film (red colour represents crystals and green represents void volume) (scale bar is 100 microns).

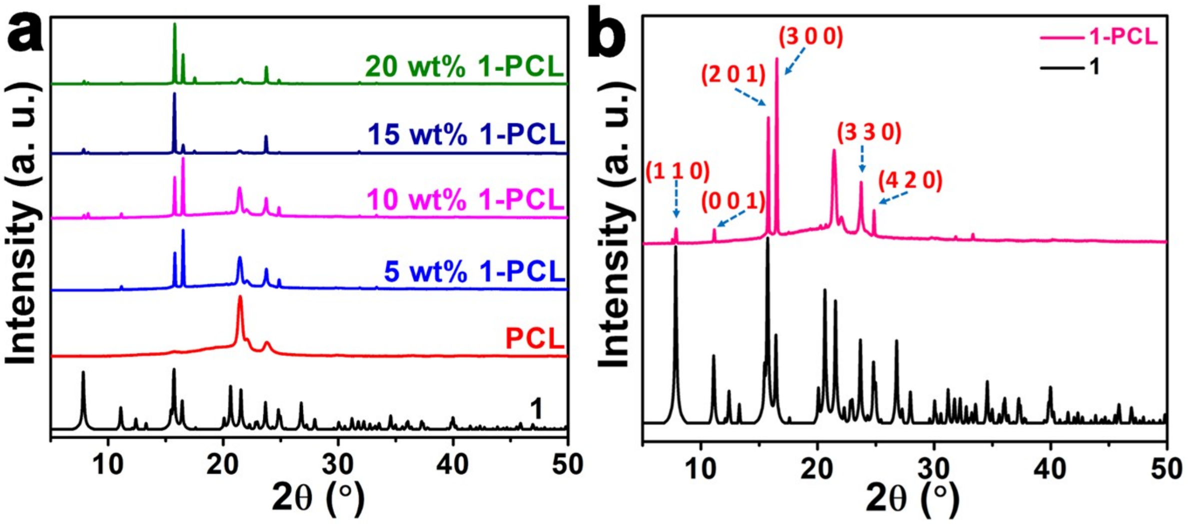

Figure S30. The powder X-ray diffraction pattern and the characteristic *hkl* peaks for compound **1** and **1**-PCL composite film.

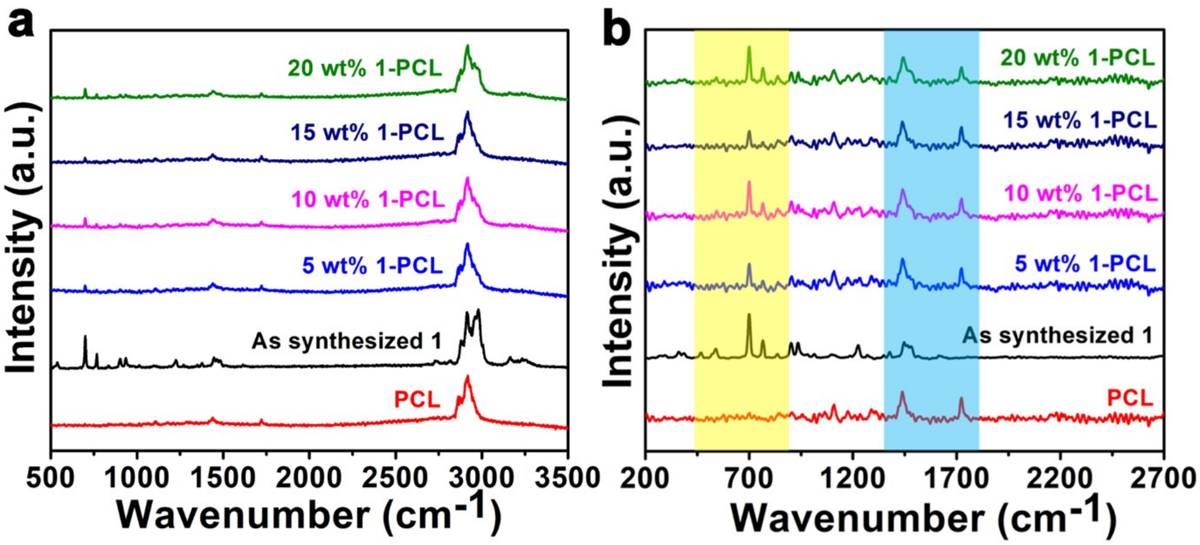

Figure S31. Raman spectral profile of all the wt% **1**-PCL composite films compared to that of the neat compound **1** and polymer PCL.

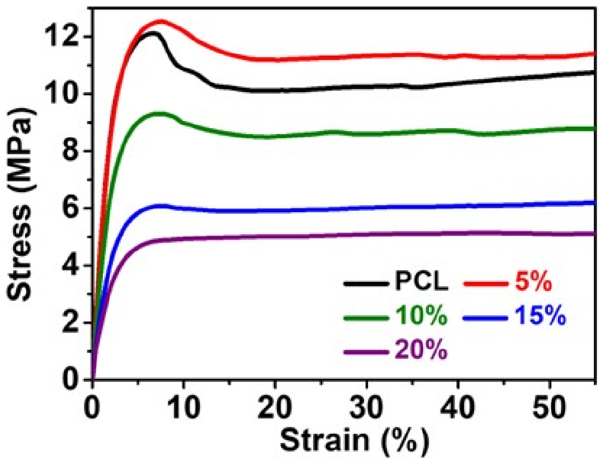

Figure S32. The stress-strain profile of PCL and **1**-PCL composite films.

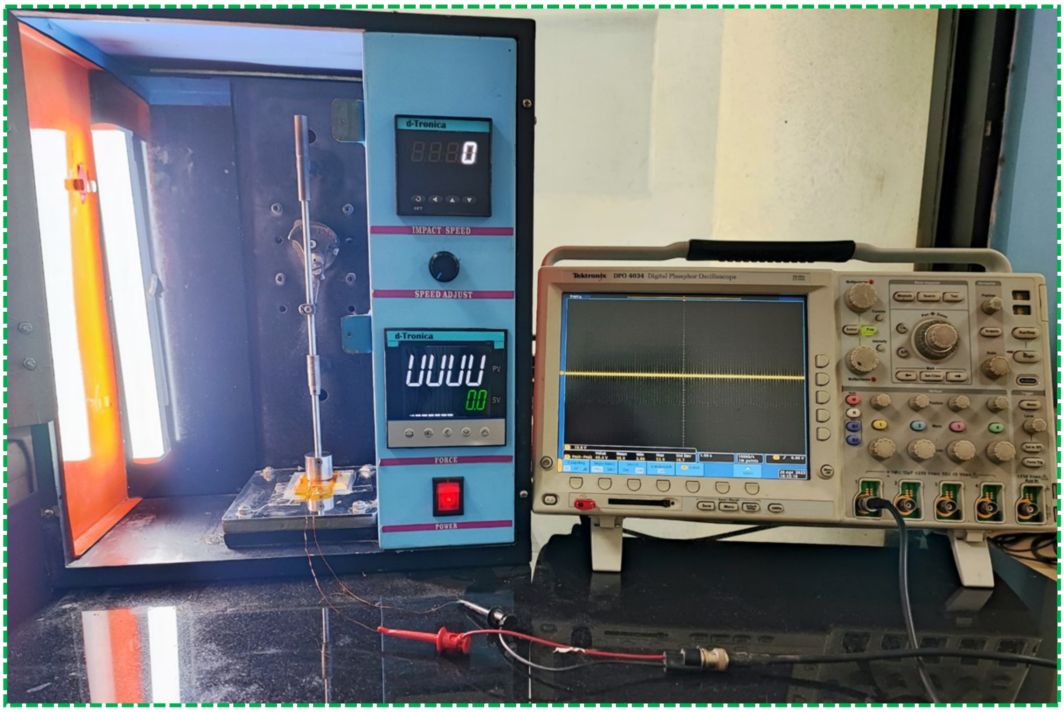

Figure S33. Picture of the piezoelectric energy harvesting setup.

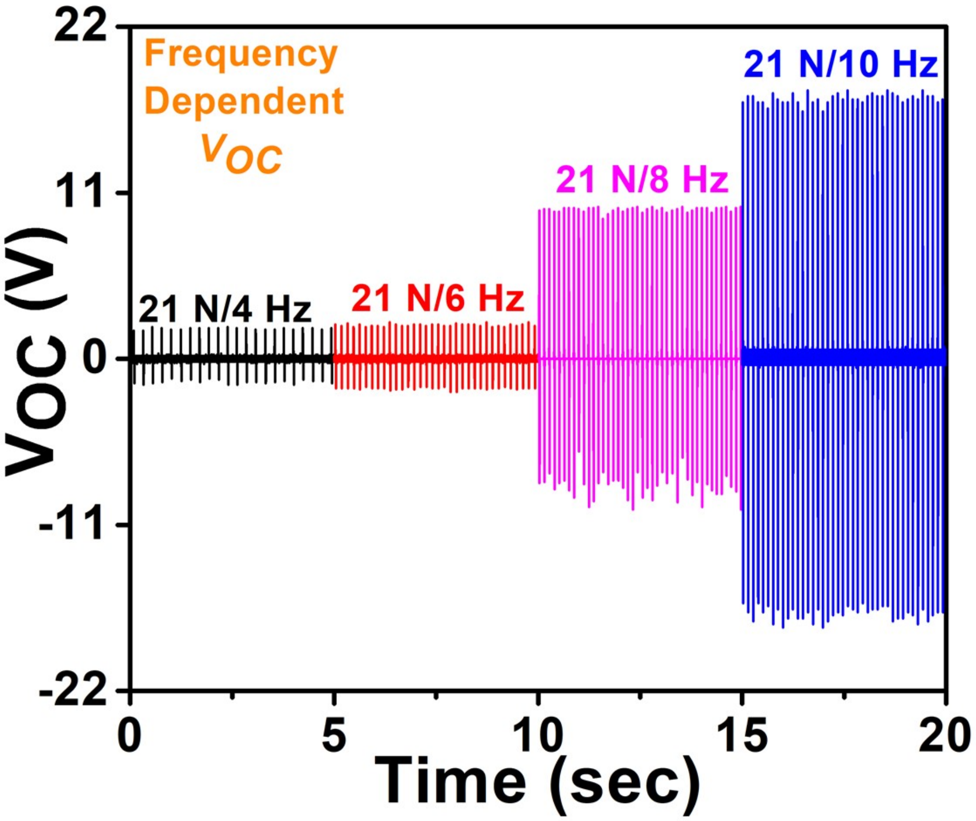

Figure S34. Frequency dependent $V_{OC\text{-}PP}$ of 10 wt% **1**-PCL under 21N applied force.

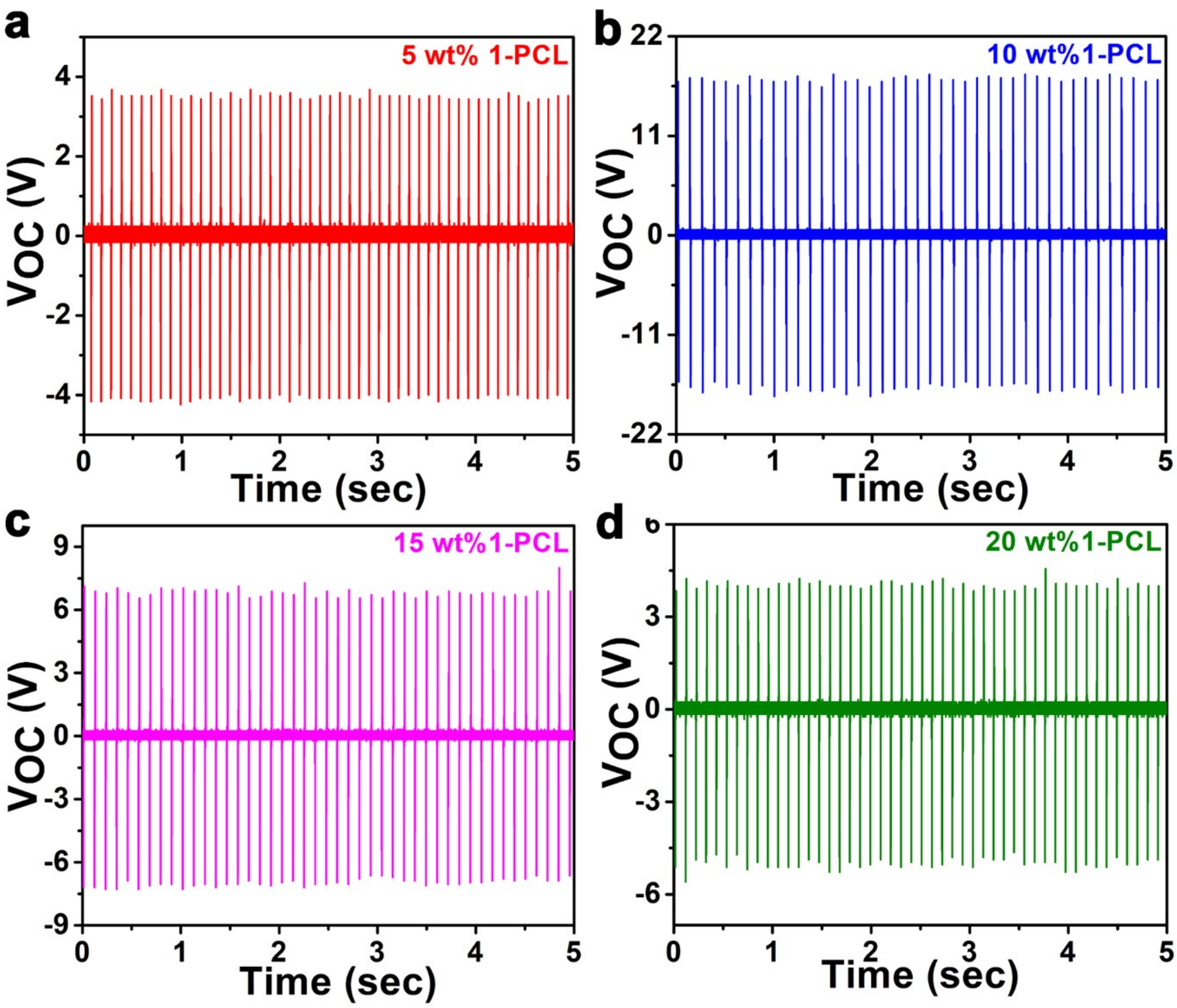

Figure S35. Output voltage profiles of **1**-PCL composite devices.

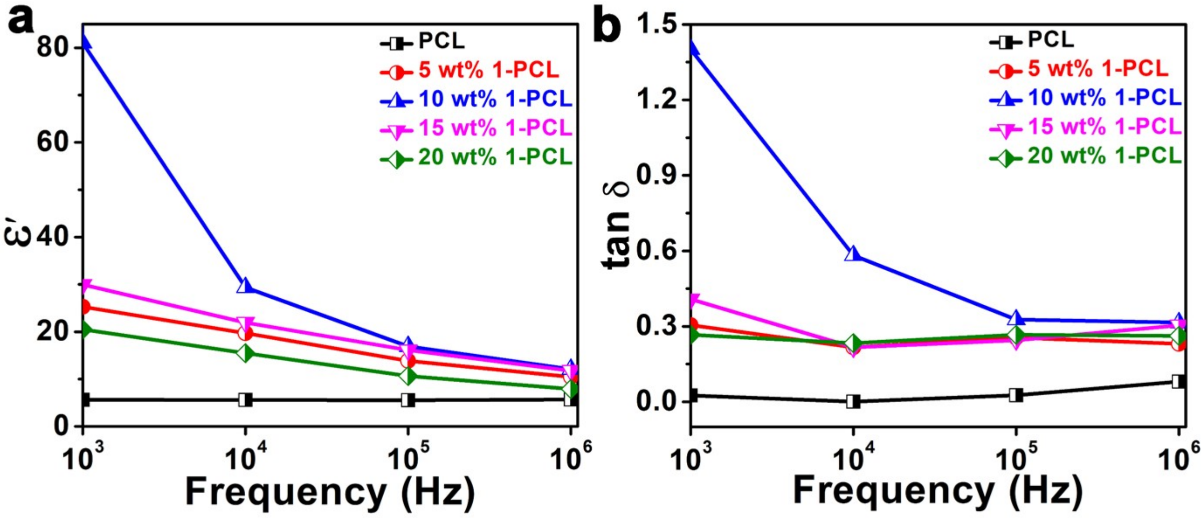

Figure S36. Frequency dependant (a) real-part of dielectric permittivity and (b) dielectric loss data for all **1**-PCL composite films.

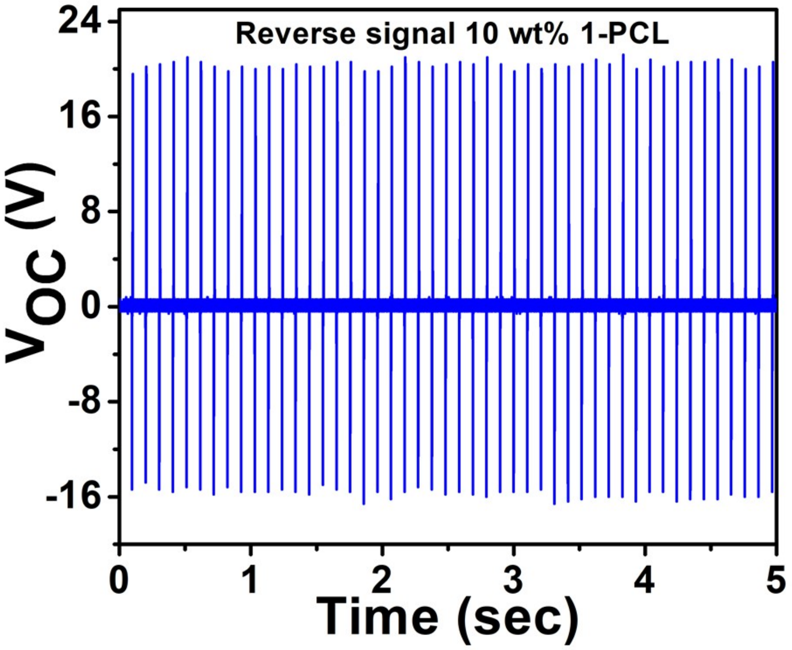

Figure S37. The polarity-switching profile of 10 wt% **1**-PCL device.

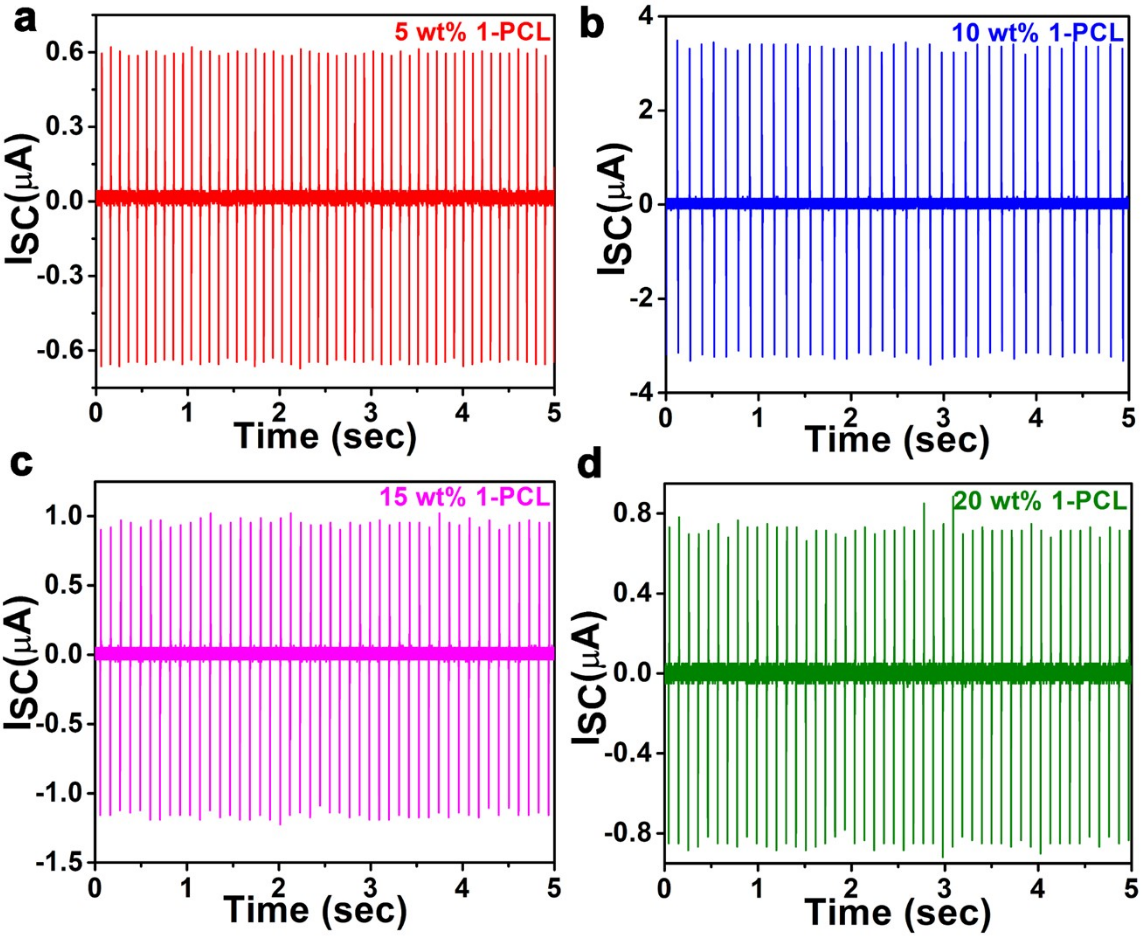

Figure S38. The calculated output currents of all **1**-PCL composite devices.

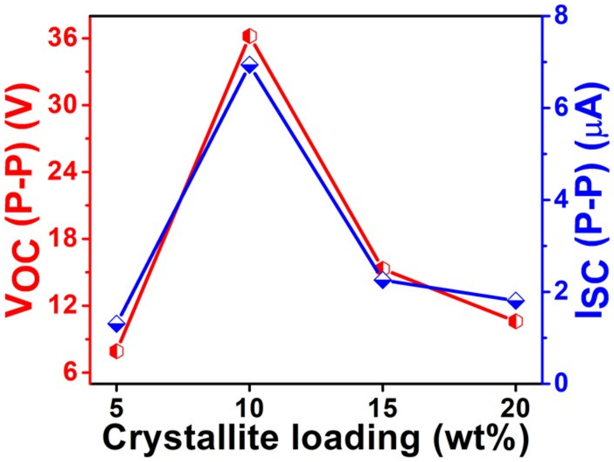

Figure S39. Comparative diagram showing the observed trends in $V_{OC\text{-}PP}$ and I_{PP} values of **1**-PCL composite devices.

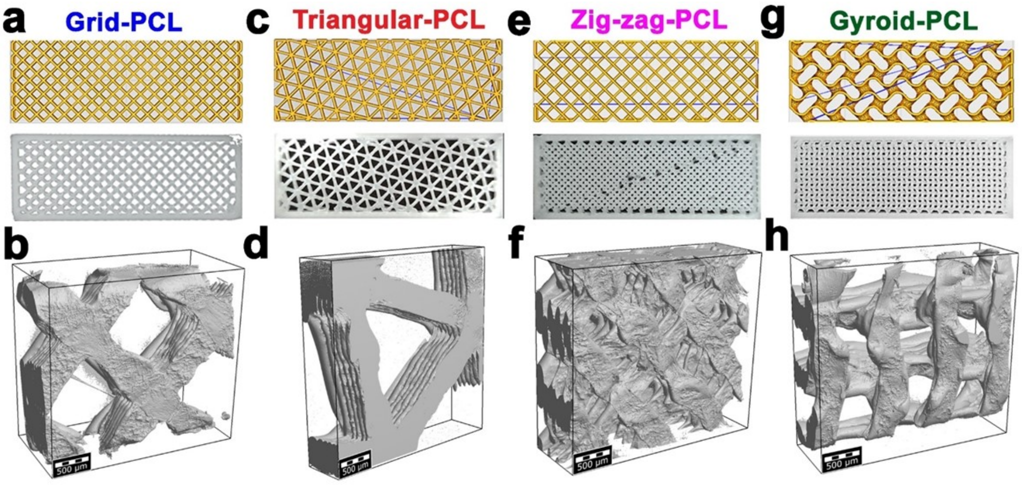

Figure S40. The computerised pictorial representations and as made 3D-printed patterns of (a) Grid-PCL (c) Triangular-PCL (e) Zig-zag-PCL (g) Gyroid-PCL and the X-ray 3D-microtomography visualisation of (b) Grid-PCL (d) Triangular-PCL (f) Zig-zag-PCL (h) Gyroid-PCL 3D-printed shapes (scale bar is 500 microns).

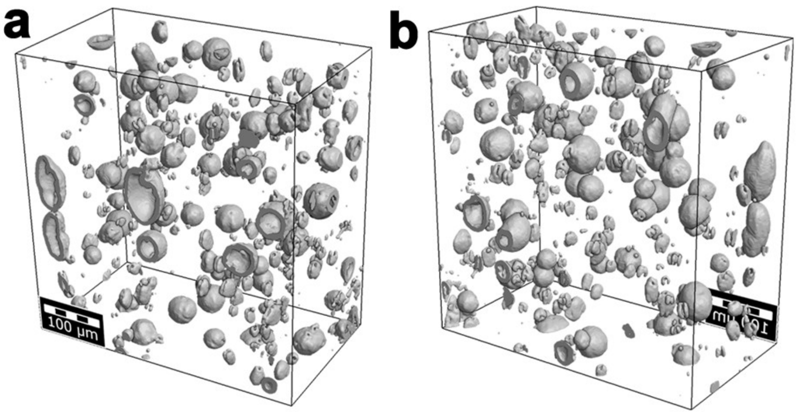

Figure S41. (a) and (b) The X-ray 3D-microtomography visualisation of the **1** crystallites in the 3D-printed ***Gy*-1**-PCL composite from the two opposite sides (the polymer background was corrected to visualize the spatial distribution of the crystallites of **1**) (scale bar is 100 microns).

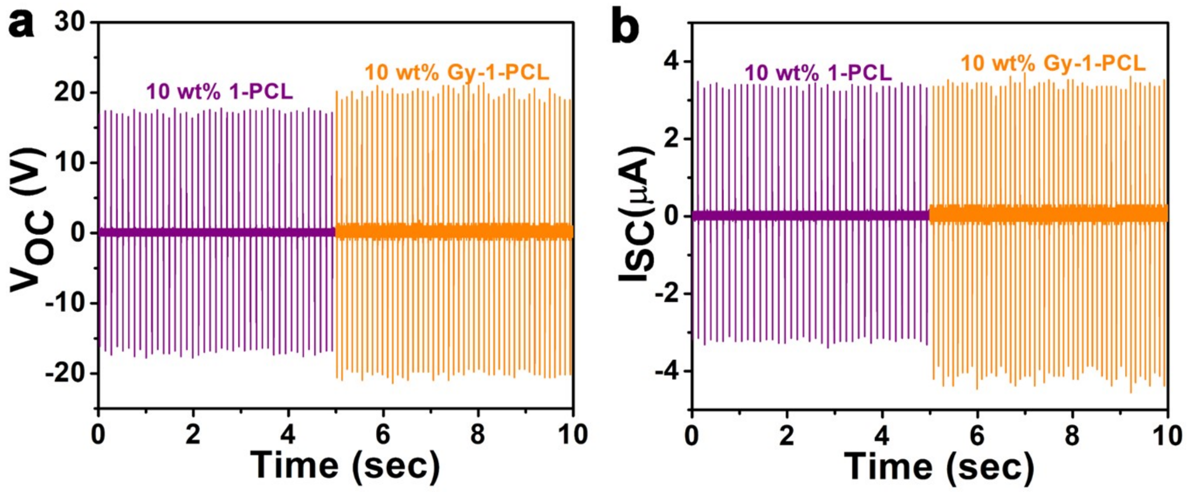

Figure S42. The comparative (a) open-circuit voltage ($V_{OC\text{-}PP}$) and (b) calculated current (I_{PP}) profiles of 3D printed 10 wt% ***Gy*-1**-PCL to that of 10 wt% **1**-PCL thin film.

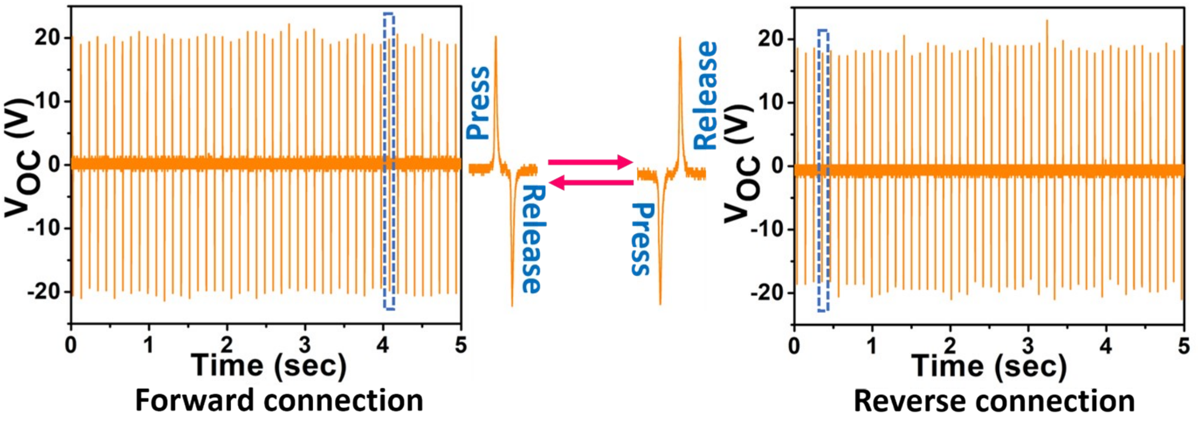

Figure S43. The polarity-switching profile of 10 wt% ***Gy*-1**-PCL.

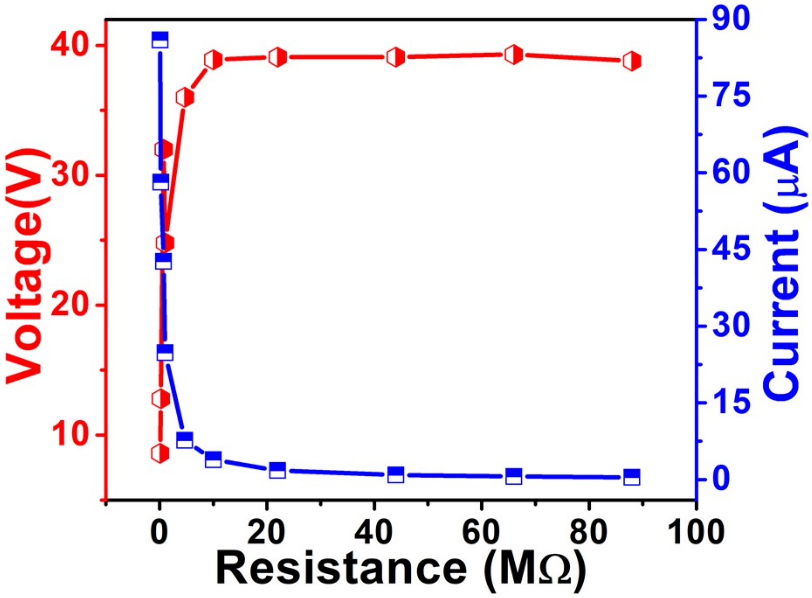

Figure S44. The comparative output voltage and current data for 10 wt% ***Gy*-1**-PCL composite device under various load resistances.

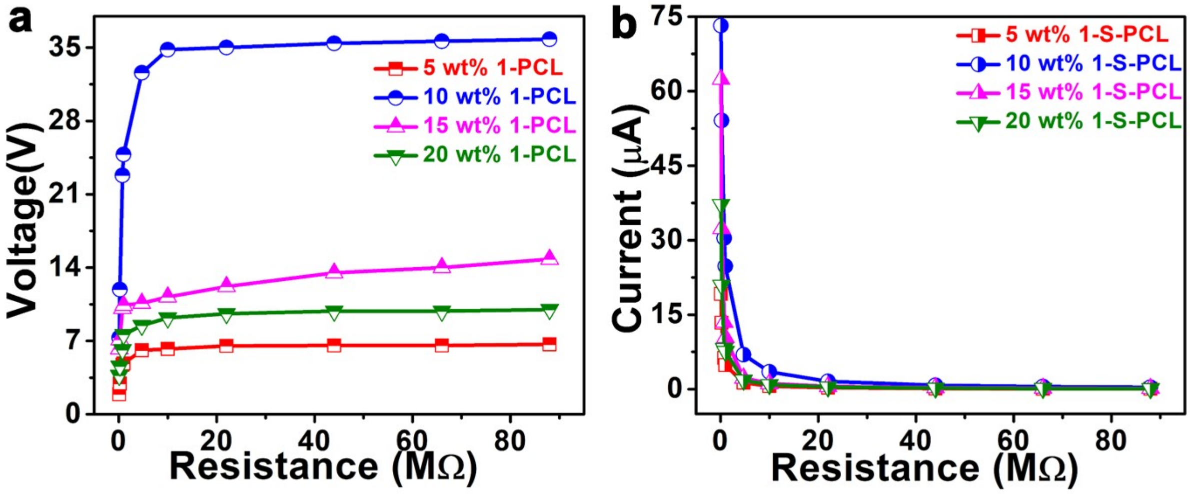

Figure S45. The comparative output (a) voltage and (b) current data for all the **1**-PCL composite devices under various load resistances.

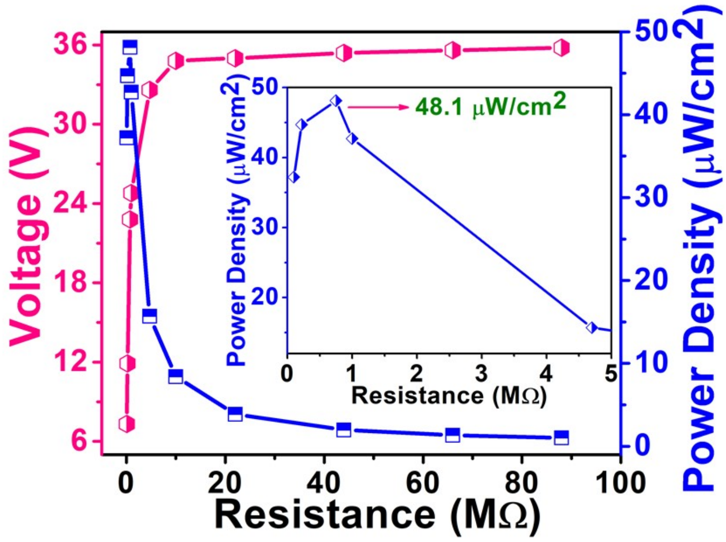

Figure S46. Voltage (V) and power density (PD) values of the 10 wt% **1**-PCL composite device under different load resistances. The inset shows magnified view of the PD profile in the low resistance region showing the maximum value at 760 kΩ.

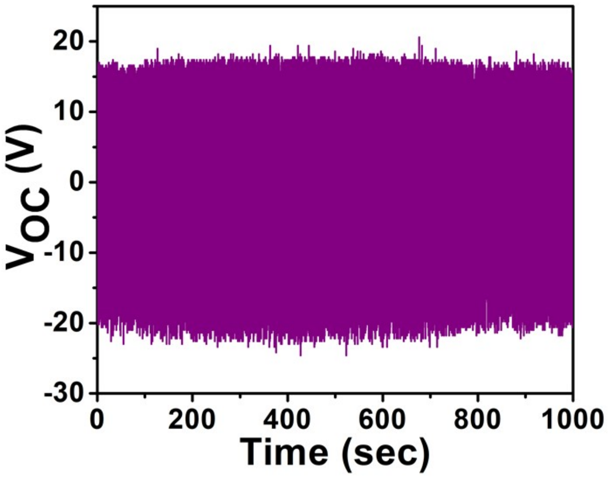

Figure S47. The cyclic stability test of 10 wt% ***Gy*-1**-PCL.

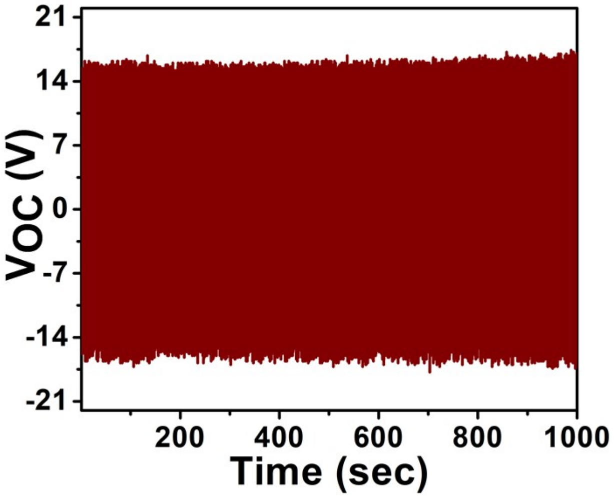

Figure S48. The cyclic stability test of 10 wt% **1**-PCL.

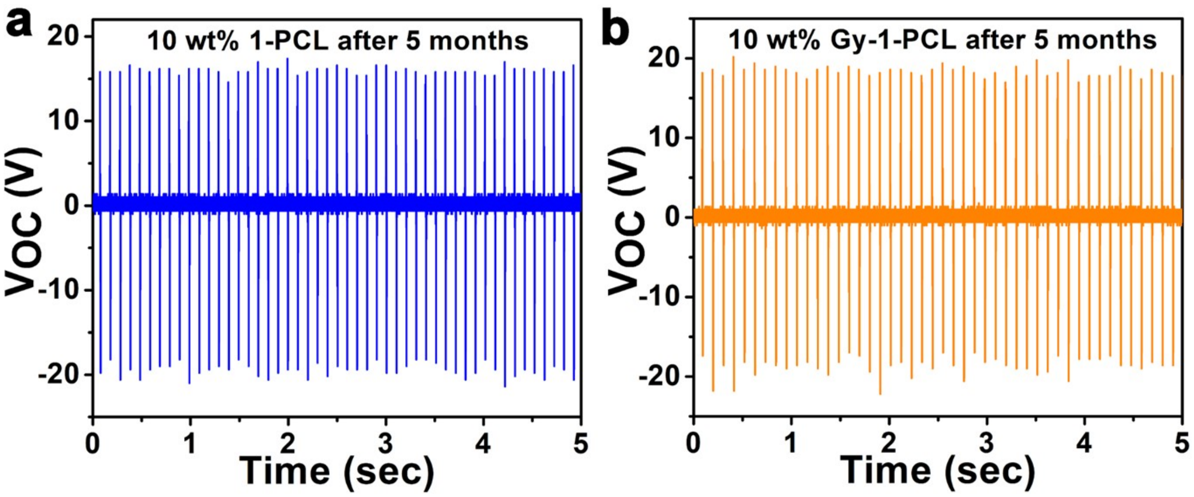

Figure S49. Reproducibility of $V_{OC\text{-}PP}$ of the 10 wt% **1**-PCL and 10 wt% ***Gy*-1**-PCL devices after 5 months.

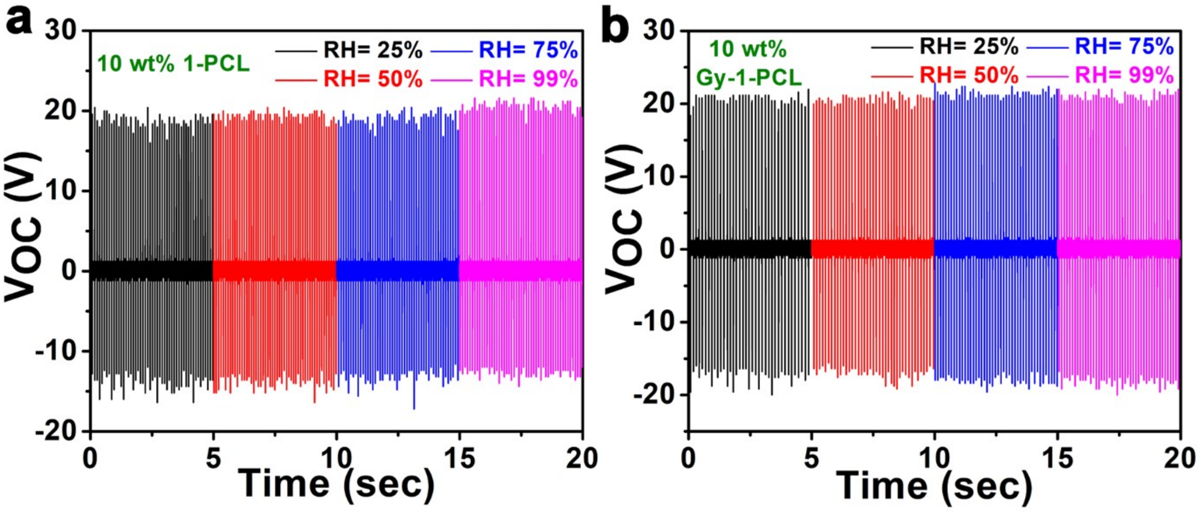

Figure S50. $V_{OC\text{-}PP}$ of 10 wt% **1**-PCL and 10 wt% ***Gy*-1**-PCL under different humid environments at 298 K.

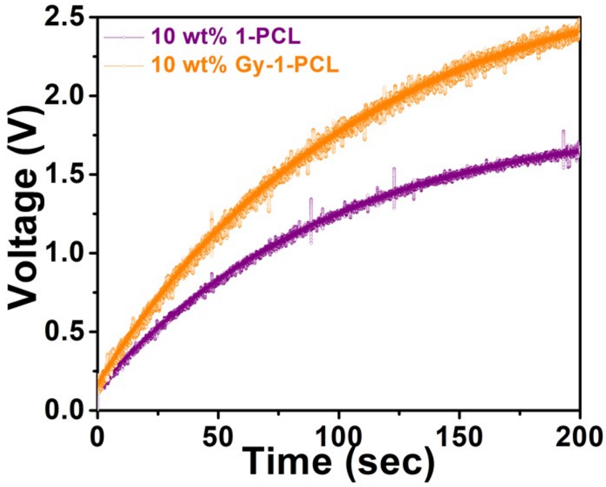

Figure S51. The voltages stored in a 100 μF capacitor by using the 10 wt% ***Gy*-1**-PCL and 10 wt% **1**-PCL devices.

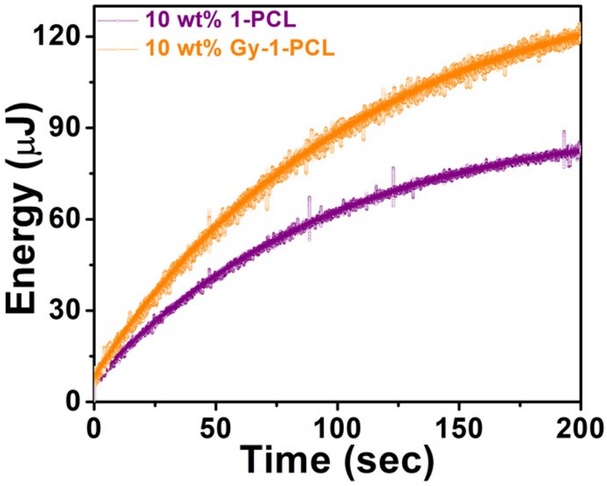

Figure S52. The energies stored in a 100 μF capacitor by using the 10 wt% ***Gy*-1**-PCL and 10 wt% **1**-PCL devices.

Table S7. Comparison of output device performances of known composite energy harvesters made from organic and hybrid compounds.

Organic Composite Devices	**Output Voltages**	**Current/Current density**	**Power/Power density**	**Active area**	**References**
DPDP·PF_6/PDMS	8.5 V	0.28 μA cm^{-2}	0.14 μW cm^{-2}	1.8 x 1 cm^2	**4**
DPDP·PF_6/TPU	6.73 V	0.12 μA cm^{-2}	0.06 μW cm^{-2}	1.3 x 3 cm^2	**5**
DPDP·BF_4/TPU	8.95 V	0.23 μA cm^{-2}	0.20 μW cm^{-2}	1.3 x 3 cm^2	**5**
TPAP·BF_4/TPU	7.37 V	0.16 μA cm^{-2}	0.09 μW cm^{-2}	1.3 x 3 cm^2	**5**
TIAP·BF_4/TPU	4.75 V	0.11 μA cm^{-2}	0.04 μW cm^{-2}	1.3 x 3 cm^2	**5**
TMAB	10 V	4.46 μA	-	-	**6**
[Bn(4-BrBn)NMe_2].BF_4	20 V	4 μA	21.1 μW cm^{-2}	1750 mm^2	**7**
3NA@PCL	7 V	70 nA	21.1 nW cm^{-2}	4.0 cm^2	**8**

Boc-FF_PCL	22 V	-	-	4.0 cm^2	**9**
Boc-FF_PLLA	8 V	-	-	4.0 cm^2	**9**
Boc-FF_PMMA	8 V	-	-	4.0 cm^2	**9**
$[Ph_3PMe]_4[CuCl_4]$	25 V	1.1 μA cm^{-2}	14.1 μW cm^{-2}	1.2 x 3 cm^2	**10**
$\{[^{s}CH(MePh)(Me)NH_3][BiBr_5]\}_n$	10.4 V	0.5 μA cm^{-2}	5.26 μW cm^{-2}	1.2 x 3 cm^2	**11**
$[Ph_3MeP]_4[Ni(NCS)_6]$/TPU	19.29 V	3.59 μA cm^{-2}	2.51 mW cm^{-3} (50.26 μW cm^{-2})	1.3 x 3 cm^2	**12**
(TMFM)$FeBr_4$	2.2 V	-	-	-	**13**
$[BnNMe_3]_2CdBr_4$/PDMS	52.9 V	0.23 μA cm^{-2}	13.8 μW cm^{-2}	3 x 3 cm^2	**14**
$[BnNMe_2{}^{n}Pr]_2CdBr_4$/PDMS	63.8 V	0.59 μA cm^{-2}	37.1 μW cm^{-2}	3 x 3 cm^2	**14**
$MAPbBr_3$-PVDF	5 V	60 nA	0.28 μW cm^{-2}	2.4 x 1.5 cm^2	**15**
$FAPbBr_3$/PVDF	26.2 V	2.1 μA	18.4 μW cm^{-2}	3 cm^2	**16**
$FAPbBr_3$–PDMS	8.5 V	3.4 μA cm^{-2}	12 μW cm^{-2}	1 x 3 cm^2	**17**
$CsPbBr_3$@PVDF	103 V	170 μA cm^{-2}	14 μW cm^{-2}	0.80 cm^2	**18**
$MASnI_3$-PVDF	12 V	4.0 μA cm^{-2}	21.6 μW cm^{-2}	1 x 1 cm^2	**19**
PVDF–PLLA–SnO_2 NF–$MAPbI_3$	4.82 V	29.7 nA	-	0.25 x 0.25 cm^2	**20**
SnO_2 NF–$MAPbI_3$	1.02 V	10.32 nA	-	0.25 x 0.25 cm^2	**20**
$MAPbI_3$-PVDF	9.43 V	0.76 μA cm^{-2}	-	1 x 1 cm^2	**21**
10 wt% 1-PCL	**36.2 V**	**6.9 μA**	**48.1 μW cm^{-2}**	**1.2 x 3 cm^2**	**This work**
10 wt% *Gy*-1-PCL	**41 V**	**7.6 μA**	**56.8 μW cm^{-2}**	**1.5 x 4 cm^2**	**This work**

Note: The overall energy harvesting performance of the composite devices depend on multiple factors, such as the ratio of the piezoelectric particles and the polymer used, materials dimensions (width, length and thickness), amount of piezoelectric crystallites in the film, phase purity of piezoelectric material, selection of polymer matrix, choice of electrode, active surface area between electrode and material, the magnitude of the applied mechanical force and operating frequency and the structural morphologies of the ferroelectric particles in the composite materials.

Note: DPDP·PF_6 = diphenyl diisopropylamino phosphonium hexaflurophosphate; TPU = thermoplastic polyurethane; DPDP·BF_4 = diphenyl diisopropylaminophosphonium tetrafluoro borate; TPAP·BF_4 = triphenyl isopropylaminophosphonium tetrafluoro borate; TIAP·BF_4 = tetraisopropylaminophosphonium tetrafluoro borate; TMAB = trimethylamine borane; PCL = polycaprolactone; PLLA= poly-l-lactic acid; PMMA = poly (methyl methacrylate); $MAPbI_3$ = methylammonium lead iodide; PVDF = polyvinylidene difluoride; PDMS = polydimethysiloxane; $FAPbBr_3$ = formamidinium lead bromide; PLLA = poly(L-lactic acid); SnO_2 = tin oxide; NF = nanofiber; $[BnNMe_3]_2CdBr_4$ = N,N,N-trimethyl-1-phenylmethanaminium cadmium(II) bromide; $[BnNMe_2{}^{n}Pr]_2CdBr_4$ = N-benzyl-N,N-dimethylpropan-1-aminium cadmium(II) bromide; (TMFM)$FeBr_4$ = trimethylfluoromethylammonium iron(III)bromide.

References

1. Sheldrick, G., A short history of SHELX. *Acta Crystallogr. A* **2008**, *64*, 112-122.
2. Spek, A., Structure validation in chemical crystallography. *Acta Crystallogr. D* **2009**, *65*, 148-155.
3. Frisch, M. J., Gaussian 03 Rev. E. 01. *http://www.gaussian. com/***2004**.
4. Vijayakanth, T.; Srivastava, A. K.; Ram, F.; Kulkarni, P.; Shanmuganathan, K.; Praveenkumar, B.; Boomishankar, R., A Flexible Composite Mechanical Energy Harvester from a Ferroelectric Organoamino Phosphonium Salt. *Angew. Chem. Int. Ed.* **2018**, *57*, 9054-9058.
5. Vijayakanth, T.; Ram, F.; Praveenkumar, B.; Shanmuganathan, K.; Boomishankar, R., All-Organic Composites of Ferro- and Piezoelectric Phosphonium Salts for Mechanical Energy Harvesting Application. *Chem. Mater.* **2019**, *31*, 5964-5972.
6. Zhang, Y.; Hopkins, M. A.; Liptrot, D. J.; Khanbareh, H.; Groen, P.; Zhou, X.; Zhang, D.; Bao, Y.; Zhou, K.; Bowen, C. R.; Carbery, D. R., Harnessing Plasticity in an Amine-Borane as a Piezoelectric and Pyroelectric Flexible Film. *Angew. Chem. Int. Ed.* **2020**, *59*, 7808-7812.
7. Gupta, R.; Sahoo, S.; Deswal, S.; Kothavade, P.; Dixit, P.; Zaręba, J. K.; Shanmuganathan, K.; Boomishankar, R., A Flexible Energy Harvester from an Organic Ferroelectric Ammonium Salt. *Chem. Asian J.* **2021**, *16*, 4122-4129.
8. Bernardo, C. R.; Baptista, R. M.; de Matos Gomes, E.; Lopes, P. E.; Raposo, M. M. M.; Costa, S. P.; Belsley, M. S., Anisotropic PCL nanofibers embedded with nonlinear nanocrystals as strong generators of polarized second harmonic light and piezoelectric currents. *Nanoscale Adv.* **2020**, *2*, 1206-1213.
9. Baptista, R. M.; de Matos Gomes, E.; Raposo, M. M. M.; Costa, S. P.; Lopes, P. E.; Almeida, B.; Belsley, M. S., Self-assembly of dipeptide Boc-diphenylalanine nanotubes inside electrospun polymeric fibers with strong piezoelectric response. *Nanoscale Adv.* **2019**, *1*, 4339-4346.
10. Sahoo, S.; Vijayakanth, T.; Kothavade, P.; Dixit, P.; Zaręba, J. K.; Shanmuganathan, K.; Boomishankar, R., Ferroelectricity and Piezoelectric Energy Harvesting of Hybrid A2BX4-Type Halogenocuprates Stabilized by Phosphonium Cations. *ACS Mater. Au* **2022**, *2*, 124-131.
11. Sahoo, S.; Deka, N.; Boomishankar, R., Piezoelectric energy harvesting of a bismuth halide perovskite stabilised by chiral ammonium cations. *CrystEngComm* **2022**, *24*, 6172-6177.
12. Vijayakanth, T.; Ram, F.; Praveenkumar, B.; Shanmuganathan, K.; Boomishankar, R., Piezoelectric Energy Harvesting from a Ferroelectric Hybrid Salt $[Ph_3MeP]_4[Ni(NCS)_6]$ Embedded in a Polymer Matrix. *Angew. Chem. Int. Ed.* **2020**, *59*, 10368-10373.
13. Zhang, Y.; Song, X.-J.; Zhang, Z.-X.; Fu, D.-W.; Xiong, R.-G., Piezoelectric Energy Harvesting Based on Multiaxial Ferroelectrics by Precise Molecular Design. *Matter* **2020**, *2*, 697-710.
14. Deswal, S.; Singh, S. K.; Rambabu, P.; Kulkarni, P.; Vaitheeswaran, G.; Praveenkumar, B.; Ogale, S.; Boomishankar, R., Flexible Composite Energy Harvesters from Ferroelectric A_2MX_4-Type Hybrid Halogenometallates. *Chem. Mater.* **2019**, *31*, 4545-4552.
15. Sultana, A.; Alam, M. M.; Sadhukhan, P.; Ghorai, U. K.; Das, S.; Middya, T. R.; Mandal, D., Organo-lead halide perovskite regulated green light emitting poly (vinylidene fluoride) electrospun nanofiber mat and its potential utility for ambient mechanical energy harvesting application. *Nano Energy* **2018**, *49*, 380-392.
16. Si, S. K.; Paria, S.; Karan, S. K.; Ojha, S.; Das, A. K.; Maitra, A.; Bera, A.; Halder, L.; De, A.; Khatua, B. B., In situ-grown organo-lead bromide perovskite-induced electroactive γ-phase in aerogel PVDF films: an efficient photoactive material for piezoelectric energy harvesting and photodetector applications. *Nanoscale* **2020**, *12*, 7214-7230.
17. Ding, R.; Liu, H.; Zhang, X.; Xiao, J.; Kishor, R.; Sun, H.; Zhu, B.; Chen, G.; Gao, F.; Feng, X., Flexible piezoelectric nanocomposite generators based on formamidinium lead halide perovskite nanoparticles. *Adv. Funct. Mater.* **2016**, *26*, 7708-7716.
18. Chen, H.; Zhou, L.; Fang, Z.; Wang, S.; Yang, T.; Zhu, L.; Hou, X.; Wang, H.; Wang, Z. L., Piezoelectric Nanogenerator Based on In Situ Growth All-Inorganic CsPbBr3 Perovskite Nanocrystals in PVDF Fibers with Long-Term Stability. *Adv. Funct. Mater.* **2021**, *31*, 2011073.
19. Jella, V.; Ippili, S.; Eom, J.-H.; Pammi, S. V. N.; Jung, J.-S.; Tran, V.-D.; Nguyen, V. H.; Kirakosyan, A.; Yun, S.; Kim, D.; Sihn, M. R.; Choi, J.; Kim, Y.-J.; Kim, H.-J.; Yoon, S.-G., A comprehensive review of

flexible piezoelectric generators based on organic-inorganic metal halide perovskites. *Nano Energy* **2019**, *57*, 74-93.

20. Tusiime, R.; Zabihi, F.; Tebyetekerwa, M.; Yousry, Y. M.; Wu, Y.; Eslamian, M.; Yang, S.; Ramakrishna, S.; Yu, M.; Zhang, H., High stress-driven voltages in net-like layer-supported organic–inorganic perovskites. *J. Mater. Chem. C* **2020**, *8*, 2643-2658.

21. Jella, V.; Ippili, S.; Eom, J.-H.; Choi, J.; Yoon, S.-G., Enhanced output performance of a flexible piezoelectric energy harvester based on stable MAPbI3-PVDF composite films. *Nano Energy* **2018**, *53*, 46-56.